Lewis-Acid Behaviour of MoF_5 and $MoOF_4$: Syntheses and Characterization of $MoF_5(NCCH_3)$, $MoF_5(NC_5H_5)_n$ and $MoOF_4(NC_5H_5)_n$ ($n = 1, 2$)

Janelle Bykowski,[a] Douglas Turnbull,[a] Nolan Hahn,[a] René T. Boeré,[a] Stacey D. Wetmore,[a] and Michael Gerken[a]*

[a] Canadian Centre for Research in Advanced Fluorine Technologies and Department of Chemistry and Biochemistry, University of Lethbridge, 4401 University Drive W, Lethbridge, AB, CA T1K 3M4

* Corresponding author. Tel.: +1-403-329-2173; Fax: +1-403-329-2057. E-mail address: michael.gerken@uleth.ca.

ABSTRACT

The Lewis acid-base adducts $MoF_5(NC_5H_5)_n$ and $MoOF_4(NC_5H_5)_n$ ($n = 1, 2$) were synthesized from reactions of MoF_5 and $MoOF_4$ with C_5H_5N and structurally characterized by X-ray crystallography. Whereas the crystal structures of $MoF_5(NC_5H_5)_2$ and $MoOF_4(NC_5H_5)_2$ are isomorphous with pentagonal bipyramidal molecules, the fluorido-bridged, heptacoordinate $[MoF_5(NC_5H_5)]_2$ dimer differs starkly from monomeric, hexacoordinate $MoOF_4(NC_5H_5)$. For the weaker Lewis base CH_3CN, only the 1:1 adduct, $MoF_5(NCCH_3)$, could be isolated. All adducts were characterized by Raman spectroscopy in conjunction with vibrational frequency calculations. Multinuclear NMR spectroscopy revealed an unprecedented isomerism of $MoOF_4(NC_5H_5)_2$ in solution, with the pyridyl ligands occupying adjacent or non-adjacent positions in the equatorial plane of the pentagonal bipyramid. Paramagnetic $MoF_5(NC_5H_5)_2$ was characterized by EPR spectroscopy as a dispersion in solid adamantane as well as in a diamagnetic host lattice of $MoOF_4(NC_5H_5)_2$; EPR parameters were computed using ZORA with the BPW91 functional using relativistic all-electron wavefunctions for Mo and simulated using EasySpin. Density functional theory (DFT) calculations (B3LYP) and NBO analyses were conducted to elucidate the distinctive bonding and structural properties of all adducts reported herein and explore fundamental differences observed in the Lewis-acid behaviour of MoF_5 and $MoOF_4$.

INTRODUCTION

The transition-metal pentafluorides, MF_5 (M = V, Nb, Ta, Cr, Mo, W, Tc, Re, Ru, Os, Rh, Ir, Pt, Au), are a unique class of highly reactive *d*-block Lewis acids with diverse Lewis-acid behaviour. Classified as moderate to strong Lewis acids, NbF_5 and TaF_5 are weaker acids than BF_3 (fluoride-ion affinity, FIA = 347.7 kJ mol^{-1})[1,2] whereas AuF_5 is a Lewis superacid (FIA = 590.8 kJ mol^{-1}).[3] The Lewis-acid behaviour of NbF_5 and TaF_5 has been investigated most extensively, and various molecular and ionic adducts have been prepared with hard or soft bases with pnictogen- or chalcogen-donor atoms (including N, O, P, S, As, Se, and Te).[4,5] Depending on the type and amount of base used, neutral adducts or, more commonly, ionic complexes containing $[NbF_4]^+$ and $[TaF_4]^+$ moieties are obtained.[5] In contrast, neutral-ligand complexes of the other *d*-block pentafluorides remain elusive. This discrepancy is largely due to synthetic challenges encountered in the preparation of later *d*-block fluorides, as well as limitations imposed by their stronger oxidative power, which render them incompatible with organic substrates.

Although improved geometric, thermodynamic, and/or spectroscopic data for MoF_5 and WF_5 have been collected since their first published syntheses in 1957 and 1968, respectively,[6-9] their Lewis-acid behaviour remains poorly understood. Calculated FIAs indicate that monomeric WF_5 (FIA = 472.8 kJ mol^{-1})[10] is a slightly stronger Lewis acid than monomeric MoF_5 (FIA = 440.2 kJ mol^{-1}),[11] although both exist as fluorido-bridged tetramers in the solid state.[6,7] While MoF_5 and WF_5 are significantly stronger Lewis acids than BF_3, they are weaker than SbF_5 (FIA = 503.3 kJ mol^{-1}),[2] which has been used as the threshold for Lewis superacidity.[12]

Despite its known Lewis acidity, there are few examples of MoF_5 complexes and, other than homoleptic $[MoF_6]^-$,[13] none have been unambiguously characterized. While Mercer et al. reported syntheses for a series of neutral MoF_5 adducts including $MoF_5(L)$ (L = NH_3, $O(CH_3)_2$,

S(CH$_3$)$_2$) and MoF$_5$(L)$_2$ (L = CH$_3$CN, C$_5$H$_5$N), characterization was solely based upon IR spectroscopic studies, elemental analyses and magnetic susceptibility measurements.[14] In addition, Fuggle et al. reported syntheses for MoF$_5$(NCCH$_3$) and MoF$_5$(NCCH$_2$Cl) and characterized these adducts by elemental analyses and IR spectroscopy.[15] Interestingly, published preparations of both MoF$_5$(NCCH$_3$) and MoF$_5$(NCCH$_3$)$_2$ involve reacting the parent pentafluoride with excess CH$_3$CN.[14,15]

Oxide fluoride anions of Mo^V, i.e., [MoOF$_4$]$^-$ and [MoOF$_5$]$^{2-}$, together with the chloride equivalents, have been studied by EPR spectroscopy.[16,17] Experimental and computed[18] EPR parameters of such Mo^V species are of ongoing interest because of the relevance of Mo^V as intermediates in mononuclear molybdoenzymes.[19]

Known fluoridotungsten(V) adducts are accessed via reduction of W^{VI} and include distorted-octahedral WF$_4$\{N(CH$_2$CF$_3$)$_2$\}\{P(C$_6$H$_5$)$_3$\}[20] and pentagonal-bipyramidal WF$_5$(NC$_5$H$_5$)$_2$,[21] both of which have been crystallographically characterized. The former complex was prepared upon reaction of WF$_5$\{N(CH$_2$CF$_3$)$_2$\} with 1.5 equivalents of P(C$_6$H$_5$)$_3$ in CH$_2$Cl$_2$,[20] while WF$_5$(NC$_5$H$_5$)$_2$ was isolated upon decomposition of [WF$_5$(NC$_5$H$_5$)$_3$]$^+$ in C$_5$H$_5$N.[21] Based on partial elemental analysis and IR spectroscopic evidence, the existence of WF$_5$(NCCH$_3$) has also been reported, having been synthesized upon reduction of WF$_6$ with elemental tungsten in CH$_3$CN.[22] The isolation of molecular WF$_5$(NC$_5$H$_5$)$_2$ demonstrates versatile Lewis-acid behaviour among the *d*-block pentafluorides, as its molecular composition differs from ionic [MF$_4$(NC$_5$H$_5$)$_4$][MF$_6$] (M = Nb, Ta); formation of [WF$_4$]$^+$ requires deliberate abstraction of F$^-$ using Me$_3$SiO$_3$SCF$_3$.[23]

Perhaps the most studied class of high-oxidation-state *d*-block Lewis acids after NbF$_5$ and TaF$_5$ are the group-6 fluorides and oxide fluorides. The tungsten compounds WF$_6$, WOF$_4$, and

WO_2F_2 have been studied extensively as Lewis acids for several decades, and while MoF_6 is not yet known to form stable adducts with neutral bases, $MoOF_4$ has been of more recent interest.[5] In contrast to $[MoF_5]_4$,[6,24] $MoOF_4$ consists of distorted octahedra linked via asymmetric *cis*-fluorido bridges into infinite chains.[25] Several molecular $MoOF_4$ adducts with monodentate bases, including $MoOF_4(L)$ (L = $OP(C_6H_5)_3$, $OP(CH_3)_3$, $O(CH_2)_4$, $OS(CH_3)_2$, $HCON(CH_3)_2$), have been synthesized from $MoOF_4(NCCH_3)$, which is conveniently prepared via O/F exchange between MoF_6 and $(Me_3Si)_2O$ in CH_3CN.[26] The presence of singlets with resolved ^{95}Mo satellites in their ^{19}F NMR spectra and binomial quintets in their ^{95}Mo ($I = 5/2$, 15.9 %) NMR spectra, demonstrates that the incoming ligand occupies a coordination site *trans* to the Mo=O moiety.[26] $MoOF_4(2,2'$-bipyridine) has also been identified by microanalysis and is expected to adopt a pentagonal-bipyramidal geometry similar to the WOF_4 analogue.[26,27] While $MoOF_4(NCCH_3)$ has proven to be a valuable precursor in accessing an array of $MoOF_4$ adducts, it is particularly noteworthy that a pure C_5H_5N adduct could not be obtained via ligand substitution with CH_3CN.[26] In addition, the only neutral, discrete $MoOF_4$ complexes for which crystallographic data have been obtained are $MoOF_4(OSO)$ and $MoOF_4\{OP(C_6H_5)_3\}$.[24,26] Whereas WOF_4 forms 1:1 complexes with various soft P-donor ligands including PMe_3, $Me_2PCH_2CH_2PMe_2$, or o-$C_6H_4(PMe_2)_2$,[28] the reaction of $MoOF_4(NCCH_3)$ with such P-donor bases results in reduction of the Mo^{VI} centre.[26] The inability to form the analogous Mo adducts is not particularly surprising since $MoOF_4$ is a significantly stronger oxidant than WOF_4.[29]

Herein, we report the preparation and characterization of adducts of MoF_5 with the Lewis bases, CH_3CN and C_5H_5N, i.e., $MoF_5(NCCH_3)$, $MoF_5(NC_5H_5)_n$ ($n = 1, 2$), which represent the first conclusively characterized neutral adducts of MoF_5. For comparison, the study was extended to

the related d^0 MoOF$_4$(NC$_5$H$_5$)$_n$ (n = 1, 2) adducts, which exhibit similarities as well as important structural differences with respect to the d^1 MoF$_5$ systems.

RESULTS AND DISCUSSION

Synthesis and Properties of MoF$_5$(NC$_5$H$_5$)$_n$, MoF$_5$(NCCH$_3$), and MoOF$_4$(NC$_5$H$_5$)$_n$ (n = 1, 2). In contrast to WF$_5$, which disproportionates into WF$_4$ and WF$_6$ at ambient or slightly elevated temperatures,[20,30] MoF$_5$ is stable at room temperature under an inert atmosphere of N$_2$. In the present study, pure MoF$_5$ was prepared upon reduction of MoF$_6$ with silicon powder in anhydrous HF (eq. 1) as previously reported,[31] although we also found that MoF$_5$ can be synthesized in quantitative yield by employing elemental tungsten powder as the reductant (eq. 2).

$$4MoF_6 + Si \rightarrow 4MoF_5 + SiF_4 \qquad (1)$$

$$6MoF_6 + W \rightarrow 6MoF_5 + WF_6 \qquad (2)$$

For the preparation of adducts, reactions were carried out at low temperature close to the melting point of the respective solvent in order to avoid any potential decomposition. To prepare MoF$_5$(NC$_5$H$_5$)$_2$, MoF$_5$ was reacted with two equivalents of C$_5$H$_5$N in CH$_2$Cl$_2$ at -85 °C or with excess C$_5$H$_5$N at -35 °C (eq. 3). The pale pink powder obtained was stable over several months at room temperature without decomposition, as verified by Raman spectroscopy. MoF$_5$(NC$_5$H$_5$)$_2$ was found to be non-volatile at 65 °C and is sparingly soluble in C$_5$H$_5$N, CH$_2$Cl$_2$, or CH$_3$CN at -35 °C, decomposing in CH$_3$CN upon heating to 40 °C. Slow hydrolysis of MoF$_5$(NC$_5$H$_5$)$_2$ in CH$_3$CN by trace amounts of water diffusing through the fluoroplastic sample tube (eq. 4) over six weeks at -35 °C yielded yellow plates that were identified as [C$_5$H$_5$NH]$_3$[Mo$_2$O$_2$F$_9$] via X-ray crystallography (*vide infra*).

$$MoF_5 + nC_5H_5N \rightarrow MoF_5(NC_5H_5)_n \quad (n = 1, 2) \qquad (3)$$

$$2MoF_5(NC_5H_5)_2 + 2H_2O \rightarrow [C_5H_5NH]_3[Mo_2O_2F_9] + [C_5H_5NH]F \qquad (4)$$
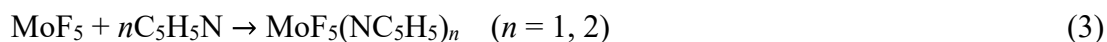
The 1:1 adduct $MoF_5(NC_5H_5)$ was prepared upon reaction of MoF_5 with one equivalent of C_5H_5N in CH_2Cl_2 at -90 °C. A transient violet solution was immediately formed when C_5H_5N initially contacted the MoF_5, although it transitioned to an orange solution as MoF_5 was consumed (Figure S1). Removal of the volatile materials under dynamic vacuum afforded a green powder, which gradually decomposed into an unidentified white solid under an inert atmosphere of N_2 within weeks at room temperature. The 1:1 adduct is highly soluble in CH_2Cl_2 or CH_3CN, affording a bright orange solution upon dissolution in either solvent, and was shown to be dimeric in the solid state by X-ray crystallography (*vide infra*). While the difference in colour between solutions and solid $MoF_5(NC_5H_5)$ might suggest a chemical transformation, such as monomerization in solution, no evidence for monomeric $MoF_5(NC_5H_5)$ could be obtained.

The reaction of MoF_5 with excess CH_3CN at -40 °C afforded a colourless solution (eq. 5), and removal of the volatile materials under dynamic vacuum resulted in the precipitation of a cream-coloured powder that was identified as $MoF_5(NCCH_3)$ by mass balance, as well as Raman spectroscopy in combination with vibrational frequency calculations. While Fuggle et al. and Mercer et al. previously reported the formation of $MoF_5(NCCH_3)$ and $MoF_5(NCCH_3)_2$, respectively, using the same synthetic approach,[14,15] the preparation of pure $MoF_5(NCCH_3)$ in the present study suggests that the donor strength of CH_3CN is not sufficient for 1:2 adduct formation to occur.

$$MoF_5 + CH_3CN \rightarrow MoF_5(NCCH_3) \tag{5}$$

Upon reaction of $MoOF_4$ with excess C_5H_5N at -35 °C, a greenish-yellow material corresponding to $MoOF_4(NC_5H_5)$ (*vide infra*) was immediately observed. Further reaction progression yielded a white suspension, and removal of the volatile materials afforded a white powder that was identified as $MoOF_4(NC_5H_5)_2$ (eq. 6). Similar to the tungsten congener,[32]

MoOF$_4$(NC$_5$H$_5$)$_2$ has low solubility in C$_5$H$_5$N at room temperature. However, the adduct was found to have a much higher solubility in SO$_2$, readily dissociating into MoOF$_4$(NC$_5$H$_5$). In addition, MoOF$_4$(NC$_5$H$_5$)$_2$ decomposes into MoOF$_4$(NC$_5$H$_5$) at room temperature *in vacuo*. A similar behaviour has been reported for WOF$_4$(NC$_5$H$_5$)$_2$ over several days,[32] and pyridine liberation is expected to be more facile for MoOF$_4$(NC$_5$H$_5$)$_2$ due to the weaker Lewis acidity of the parent oxide fluoride (MoOF$_4$: FIA = 355; WOF$_4$: FIA = 386 kJ mol^{-1})[33].

$$MoOF_4 + nC_5H_5N \rightarrow MoOF_4(NC_5H_5)_n \quad (n = 1, 2) \tag{6}$$
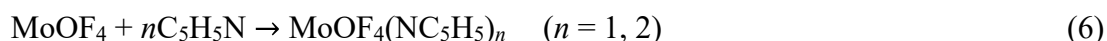
While a colourless solution immediately formed upon reaction of MoOF$_4$ with one equivalent of C$_5$H$_5$N in CH$_2$Cl$_2$ at −75 °C, removal of the volatile materials afforded a viscous green material that readily sublimed *in vacuo* at room temperature, yielding a thin white residue that coated the walls of the FEP vessel. Raman data collected from multiple preparations of MoOF$_4$(NC$_5$H$_5$) indicated that an impurity of MoOF$_4$(NC$_5$H$_5$)$_2$ was consistently present, which accounts for the broad melting point of the green material (ca. 3 to −15 °C). To ensure that the viscous, gel-like appearance of the product was not attributable to thermal decomposition, one preparation of MoOF$_4$(NC$_5$H$_5$) involved maintaining the temperature of the reactor below −40 °C for the entire synthesis and recording a Raman spectrum of the green crystalline solid at −100 °C immediately following the removal of the volatile materials under dynamic vacuum. The Raman spectrum recorded at −100 °C was identical to the spectra recorded at room temperature, which demonstrates that decomposition is not responsible for the appearance of the product. Interestingly, the ratio of MoOF$_4$(NC$_5$H$_5$) to MoOF$_4$(NC$_5$H$_5$)$_2$ increased after storing the green material over several weeks at −70 °C, although attempts to isolate pure MoOF$_4$(NC$_5$H$_5$) by expediting the sublimation process under dynamic vacuum were not successful.

Molecular Geometries. The structures of $MoF_5(NC_5H_5)_n$, $MoOF_4(NC_5H_5)_n$ and $[C_5H_5NH]_3[Mo_2O_2F_9]$ were studied via single-crystal X-ray diffraction, and gas-phase geometry optimizations (DFT/B3LYP) were also performed for all adducts reported herein. Crystallographic data and refinement parameters are presented in Table 1, along with selected experimental and calculated bond lengths and angles in Tables 2-4 and Tables S1-S3. The experimental metric parameters are in close agreement with the calculated values, although the Mo–N bond lengths in the optimized geometries are slightly overestimated (by up to 0.103 Å) for all adducts investigated.

Table 1. Crystallographic Data Collection and Refinement Parameters for, MoF$_5$(NC$_5$H$_5$)$_n$, MoOF$_4$(NC$_5$H$_5$)$_n$ (n = 1, 2), and [C$_5$H$_5$NH]$_3$[Mo$_2$O$_2$F$_9$].

Compound	MoF$_5$(NC$_5$H$_5$)$_2$	[MoF$_5$(NC$_5$H$_5$)]$_2$	MoOF$_4$(NC$_5$H$_5$)$_2$	MoOF$_4$(NC$_5$H$_5$)	[C$_5$H$_5$NH]$_3$[Mo$_2$O$_2$F$_9$]
Chemical formula	C$_{10}$H$_{10}$F$_5$MoN$_2$	C$_{10}$H$_{10}$F$_{10}$Mo$_2$N$_2$	C$_{10}$H$_{10}$F$_4$MoN$_2$O	C$_5$H$_5$F$_4$MoNO	C$_{15}$H$_{18}$F$_9$Mo$_2$N$_3$O$_2$
Formula weight	349.14	540.08	346.14	267.04	635.20
Temperature (°C)	–173	–173	–173	–173	–173
Crystal system	monoclinic	triclinic	monoclinic	orthorhombic	triclinic
Space group	$C2/c$	$P\bar{1}$	$C2/c$	$Pbcn$	$P\bar{1}$
a (Å)	8.1518(3)	6.7695(3)	8.1541(5)	14.0142(9)	7.9204(2)
b (Å)	11.0827(4)	7.5886(3)	11.1489(6)	7.5146(5)	8.0146(2)
c (Å)	13.6414(5)	7.9383(3)	13.5051(8)	14.8676(9)	9.1661(2)
α (°)	90	79.231(3)	90	90	102.461(2)
β (°)	107.188(4)	81.450(3)	107.261(7)	90	104.590(2)
γ (°)	90	65.782(4)	90	90	104.839(2)
V (Å^3)	1177.38(8)	364.18(3)	1172.44(13)	1565.72(18)	519.30(2)
Z	4	1	4	8	1
$R_1{}^a$ [I $\geq$ 2σ(I)]	0.0207	0.0179	0.0193	0.0250	0.0201
wR$_2{}^a$ [I $\geq$ 2σ(I)]	0.0496	0.0440	0.0504	0.0541	0.0447
CCDC	2099019	2099017	2099020	2099021	2099018

$^a R_1 = \sum ||F_o| - |F_c||/\sum|F_o|. wR_2 = [\sum[w(F_o{}^2 - F_c{}^2)^2]/\sum w(F_o{}^4)]^{1/2}$.

Table 2. Selected bond lengths (Å) and angles (°) of MoF$_5$(NC$_5$H$_5$)$_2$, MoF$_5$(NCCH$_3$), and [MoF$_5$(NC$_5$H$_5$)]$_2$.

	MoF$_5$(NC$_5$H$_5$)$_2$		MoF$_5$(NCCH$_3$)
	Exptl.[a]	Calcd.[c]	Calcd.
Mo–F$_{ax}$	1.9002(12)	1.909	1.848
Mo–F$_{eq}$	1.8822(16)–1.9141(12)	1.894, 1.900	1.837, 1.891
Mo–N	2.2232(16)	2.303	2.243
F$_{ax}$–Mo–F$_{eq}$	87.05(4)–94.78(6)	85.6–96.1	90.4–100.2
F$_{ax}$–Mo–F$_{ax}$	174.09(8)	171.2	
F$_{ax}$–Mo–N	87.46(5)–90.75(6)	86.7, 90.4	180.0
N–Mo–N^{i}	144.73(8)	142.3	

	[MoF$_5$(NC$_5$H$_5$)]$_2$	
	Exptl.[b]	Calcd.[c]
Mo–F$_{ax}$	1.8759(12), 1.8865(12)	1.892
Mo–F$_t$	1.8465(11), 1.8514(12)	1.857
Mo–F$_b$	2.0740(12), 2.0786(11)	2.088
Mo–N	2.1677(16)	2.240
Mo–Mo^{ii}	3.4981(3)	3.518
F$_{ax}$–Mo–F$_t$	88.81(5)–92.15(5)	89.3, 90.5
F$_{ax}$–Mo–F$_b$	88.59(5)–90.36(5)	89.9, 90.6
F$_{ax}$–Mo–F$_{ax}$	177.31(5)	179.4
F$_{ax}$–Mo–N	90.13(6), 92.09(6)	89.7
F$_t$–Mo–F$_t$	148.18(5)	146.8
F$_t$–Mo–N	74.08(6), 74.20(6)	73.4
F$_b$–Mo–N	147.19(5), 147.54(5)	147.4
F$_b$–Mo–F$_b^{ii}$	65.21(5)	65.2
Mo–F$_b$–Mo^{ii}	114.79(5)	114.8

[a] Symmetry transformation i = 1 − x, y, $^3/_2$ − z. [b] Symmetry transformation ii = 1 − x, − y, 1 − z.

[c] Calculated at the B3LYP/aVTZ level of theory.

Table 3. Selected bond lengths (Å) and angles (°) of $MoOF_4(NC_5H_5)_n$ (n = 1, 2).

	$MoF_5(NC_5H_5)$		$MoF_5(NC_5H_5)_2$	
	Exptl.	Calcd.[a]	Exptl.[b]	Calcd.[a]
Mo–F$_{ax}$			1.8209(11)[c]	1.951
Mo–F$_{eq}$	1.8492(13)–1.8585(13)	1.864	1.9067(10), 1.9177(13)	1.895–1.938
Mo–O	1.6612(16)	1.664	1.8209(11)[c]	1.686
Mo–N	2.3472(19)	2.450	2.2265(13)	2.315, 2.318
O–Mo–F$_{eq}$	98.13(7)–98.79(7)	100.4	86.36(3)–94.32(5)	89.3–99.5
O–Mo–F$_{ax}$			172.73(7)	169.3
O–Mo–N	179.59(7)	180.0	87.53(5), 90.17(5)	89.2, 91.9
N–Mo–N^i			143.17(7)	140.8

[a] Calculated at the B3LYP/aVTZ level of theory. [b] Symmetry transformation i = 1 – x, y, ½ – z. [c] Statistically averaged due to 50/50 disorder between O and F(2).
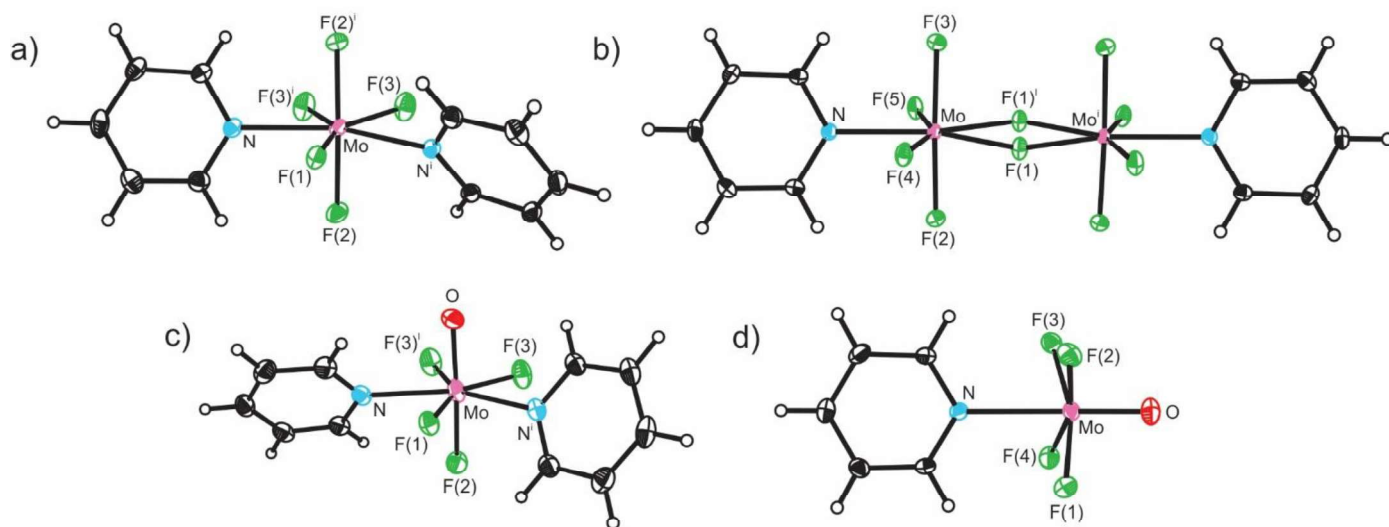
Figure 1. Thermal ellipsoid plots (50% probability level) of a) $MoF_5(NC_5H_5)_2$, b) $[MoF_5(NC_5H_5)]_2$, c) $MoOF_4(NC_5H_5)_2$, and d) $MoOF_4(NC_5H_5)$. The O and F(2) atoms in c) are disordered and were constrained to be equal.
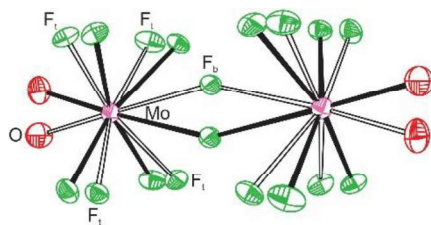
Figure 2. Thermal ellipsoid plot (50% probability level) of $[Mo_2O_2F_9]^{3-}$ in $[C_5H_5NH]_3[Mo_2O_2F_9]$. Solid and unfilled bonds represent the two components of the disorder model.
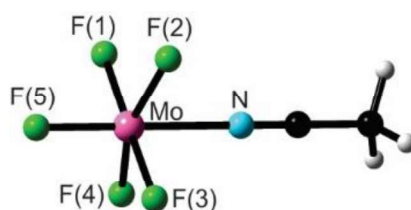
Figure 3. Optimized gas-phase geometry of $MoF_5(NCCH_3)$.

$MoF_5(NC_5H_5)_2$, $MoOF_4(NC_5H_5)_2$ and $[C_5H_5NH]_3[Mo_2O_2F_9]$. A dilute pink solution of MoF_5 in C_5H_5N, prepared upon heating to 45 °C, was rapidly cooled to −35 °C to afford red/orange blocks of $MoF_5(NC_5H_5)_2$. Similarly, $MoOF_4$ dissolved in a large excess of C_5H_5N upon gentle agitation at room temperature, and light yellow plates corresponding to $MoOF_4(NC_5H_5)_2$ formed upon slow removal of excess pyridine under dynamic vacuum at −30 °C. $MoF_5(NC_5H_5)_2$ and $MoOF_4(NC_5H_5)_2$ are isomorphous with each other and also with $WF_5(NC_5H_5)_2$[21] and $WOF_4(NC_5H_5)_2$,[34] crystallizing in the monoclinic space group $C2/c$ and adopting pentagonal bipyramidal geometries with the pyridyl ligands occupying non-adjacent coordination sites in the equatorial plane (Figures 1a,c). The experimental bond lengths and angles of $MoF_5(NC_5H_5)_2$ and $WF_5(NC_5H_5)_2$[21] differ only negligibly, and the Mo–F bond lengths in $MoF_5(NC_5H_5)_2$ (exptl.: 1.8822(16)–1.9141(12) Å; calcd.: 1.894–1.909 Å) are also comparable to those observed for $[MoF_7]^-$ (1.853(5)–1.898(5) Å in its Cs^+ salt), which exists as a monocapped octahedron.[35] While

MF$_5$ (M = Nb, Ta) undergo quantitative ligand-induced autoionization in the presence of excess C$_5$H$_5$N to afford ionic [MF$_4$(NC$_5$H$_5$)$_4$][MF$_6$],[36] the formation of a molecular adduct in the present study demonstrates that the bridging Mo–F bonds of the [MoF$_5$]$_4$ tetramer are symmetrically cleaved when exposed to excess C$_5$H$_5$N. As evidenced by electrical conductivity measurements, NbF$_5$ and TaF$_5$ autoionize in the melt to a significantly greater extent than MoF$_5$,[37] and the relative susceptibilities of the parent pentafluorides towards asymmetric cleavage of the bridging bonds in the tetramer is thus reflected in the nature of their 1:2 C$_5$H$_5$N adducts.

Similar to the tungsten congener,[34] the crystallographically imposed twofold rotation axis in MoOF$_4$(NC$_5$H$_5$)$_2$ imparts 50/50 disorder among the axial oxido and fluorido ligands, and the constrained refinement employed resulted in an averaging of the apparent Mo–O and Mo–F$_{ax}$ bond lengths of 1.8209(11) Å (calcd.: Mo–O, 1.686; Mo–F, 1.951 Å; average, 1.819 Å). The O–Mo–F$_{ax}$ bond angle (exptl.: 172.73(7)°; calcd.: 169.3°) is significantly distorted from linearity, which is similar to that observed in WOF$_4$(NC$_5$H$_5$)$_2$ ($\angle$(O–W–F$_{ax}$) = 173.60(13)°)[34] and MoF$_5$(NC$_5$H$_5$)$_2$ ($\angle$(F$_{ax}$–Mo–F$_{ax}$); exptl.: 174.09(8)°; calcd.: 171.2°).

The accidental hydrolysis product [C$_5$H$_5$NH]$_3$[Mo$_2$O$_2$F$_9$] crystallizes in the triclinic space group $P\bar{1}$ (Figure 2). The dinuclear d^1 oxidofluoridomolybdate [Mo$_2$O$_2$F$_9$]$^{3-}$ possesses a two-component disorder about the crystallographic inversion centre and adopts a distorted octahedral geometry in which the oxido ligands occupy terminal positions *trans* to the μ–F bond. The Mo−Mo distance (4.2456(3) Å) is significantly longer than that observed in [MoF$_5$(NC$_5$H$_5$)]$_2$ (3.4981(3) Å) (*vide infra*) and [MoF$_5$]$_4$ (4.0881(3) Å),[6] which suggests the absence of any significant bonding interaction between the Mo centres. While the Mo−F and Mo=O bond lengths are in agreement with those previously reported for [NH$_4$]$_3$[Mo$_2$O$_2$F$_9$] and K$_2$([N(CH$_3$)$_4$][Mo$_2$O$_2$F$_9$]·H$_2$O,[38,39] the Mo−(μ–F)−Mo bond angle (155.42(10)°) is substantially smaller than the corresponding angle in

$[NH_4]_3[Mo_2O_2F_9]$ (164.2(7)°, 180.0°) and $K_2[N(CH_3)_4][Mo_2O_2F_9]·H_2O$ (169.4(3)°) and is even slightly smaller than that observed in $Li[Mo^{VI}_2O_2F_9]$ (158.89(12)°).[25]

$MoF_5(NC_5H_5)$. Green blocks of $MoF_5(NC_5H_5)$ were grown from a concentrated solution of the adduct in CH_2Cl_2 at –55 °C. Crystallizing in the triclinic space group $P\bar{1}$ with two formula units per unit cell, the adduct exists as fluorido-bridged dimers $[MoF_5(NC_5H_5)]_2$ with each Mo^V centre adopting a pentagonal-bipyramidal geometry such that the pyridyl ligands occupy equatorial positions (Figure 1b). The 3c-4e$^-$ μ–F bonds are essentially symmetric (exptl.: 2.0740(12), 2.0786(11); calcd.: 2.088 Å) and only slightly elongated relative to those of $[MoF_5]_4$ (2.0423(11), 2.0463(11) Å).[6] The F_{ax}–Mo–F_{ax} bond angle (exptl.: 177.31(5)°; calcd.: 179.4°) closely approaches linearity, and the ten atoms situated in the equatorial plane ($Mo_2F_6N_2$) exhibit minimal deviation from the corresponding least-squares plane (≤ 0.042 Å), intersecting the least-squares plane of the two pyridyl ligands at an angle of 63.3°. Similar coordination motifs have been previously observed for $[Zr_2F_{12}]^{4-}$ in $[Co((NH_2)_2C_2H_4)_3]_2[Zr_2F_{12}][SiF_6]·4H_2O$ and for $[MF_4(OS(CH_3)_2)_2]_2$ (M = Zr, Hf).[40,41] Although the Mo–Mo distance (exptl.: 3.4981(3); calcd.: 3.518 Å) is much smaller than the sum of the van der Waals radii (R_{vdW}(Mo) = 2.1 Å),[42] the bond angles of the four-membered ring (F_b–Mo–F_b; exptl.: 65.21(5)°; calcd.: 65.2°; Mo–F_b–Mo; exptl.: 114.79(5)°; calcd.: 114.8°), the low Wiberg bond index (WBI = 0.01), and the negligible (3.3 kJ mol^{-1}) donor-acceptor interaction as determined by second-order perturbation theory of the NBO analysis collectively indicate that no significant bonding character is present between the molybdenum centres. Conversely, an appreciably smaller Mo–Mo distance (2.533(1) Å) is observed in the octahedral Mo^{III} complex $[MoF_3(NC_5H_5)_2]_2$, which thus contains a substantial bonding interaction.[43] $MoF_5(NC_5H_5)_2$, $[MoF_5(NC_5H_5)]_2$, and $MoOF_4(NC_5H_5)_2$ represent the first

15

neutral adducts of MoF_5 and the first heptacoordinate adduct of $MoOF_4$, respectively, to be conclusively characterized.

$MoOF_4(NC_5H_5)$ and $MoF_5(NCCH_3)$. In contrast to the dimerization observed for $MoF_5(NC_5H_5)$, $MoOF_4(NC_5H_5)$ and $MoF_5(NCCH_3)$ both exist as monomers in the solid state. Although no crystals suitable for crystallography were obtained for $MoF_5(NCCH_3)$, on the basis of Raman spectroscopy (*vide infra*), the octahedral coordination sphere in $MoF_5(NCCH_3)$ is expected to resemble that of $MOF_4(NCCH_3)$ (M = Mo, W), with an apical fluorine atom in place of the oxido ligand.[26,27] The excellent correlation between the experimental and calculated vibrational frequencies (Table S23) corroborates the validity of the geometry-optimized structure (Figure 3), which contains two distinct Mo–F bonds in the equatorial plane (1.837 and 1.891 Å) and a perfectly linear F_{ax}–Mo–N bond angle. In agreement with the low site symmetry (lower than C_{4v}) predicted by Fuggle et al. based on vibrational spectroscopic data,[15] the computed structural parameters indicate that the MoF_5N moiety is significantly distorted towards C_{2v} symmetry, which was also observed for the WF_4NP moiety of $WF_4\{N(CH_2CF_3)_2\}\{P(C_6H_5)_3\}$.[20] The bond angles between *trans* equatorial fluorido ligands are 179.1° and 159.7°, with the shorter Mo–F bonds being substantially bent towards the CH_3CN moiety. Similar to $MoF_5(NC_5H_5)_2$, the synthesis of a molecular adduct contrasts the known Lewis-acid behavior of NbF_5, which autoionizes in the presence of two molar equivalents of CH_3CN to afford $[NbF_4(NCCH_3)_4][NbF_6]$.[44]

Light yellow plates of $MoOF_4(NC_5H_5)$ were grown under dynamic vacuum at −55 °C from a dilute CH_2Cl_2 solution. In agreement with previously reported $MoOF_4$ adducts,[24,26] the pyridyl ligand occupies a coordination site *trans* to the oxido ligand (Figure 1d). Isomorphous with $WOF_4(NC_5H_5)$,[35] the adduct crystallizes in the orthorhombic space group *Pbcn* with eight formula units in the unit cell. The $\angle$(O–M–N) (M = Mo, W) bond angles in $MoOF_4(NC_5H_5)$ (exptl.:

179.59(7)°; calcd.: 180.0°) and $WOF_4(NC_5H_5)$ (179.73(16)°) are essentially linear,[35] and the

Mo=O (exptl.: 1.6612(16); calcd.: 1.664 Å) and Mo–F (exptl.: 1.8492(13)–1.8585(13); calcd.:

1.864 Å) bond lengths are comparable to those observed in $MoOF_4\{OP(C_6H_5)_3\}$ (1.6643(18) and

1.8490(15)–1.8704(14) Å, respectively)[26] and $MoOF_4(OSO)$ (1.6465(14) and 1.8403(10)–

1.8631(11) Å, respectively).[24] In addition, similar to these previously reported $MoOF_4(L)$ adducts,

the Mo centre is slightly displaced (0.272 Å) from the centre of the least-squares plane, defined by

the four equatorial fluorine atoms, towards the oxido ligand.

^{19}F NMR Spectroscopy. The solution-state behaviour of $MoOF_4(NC_5H_5)_n$ in CH_2Cl_2 was investigated via NMR spectroscopy. No signals corresponding to the Mo^V adducts were observed in the ^{19}F NMR spectra of $MoF_5(NCCH_3)$ or $MoF_5(NC_5H_5)_n$, which is consistent with the paramagnetism imparted by the d^1 electron configurations. For $MoOF_4(NC_5H_5)$, the ^{19}F NMR spectrum contains a singlet at 141.50 ppm, and ^{95}Mo satellites ($I = 5/2$, 15.9 %) with a $^1J(^{95}Mo-$ $^{19}F)$ coupling constant of 68.8 Hz (Figure 4). The magnitude of the observed coupling constant closely agrees with those reported for previously studied $MoOF_4(L)$ complexes (62-67 Hz).[26]
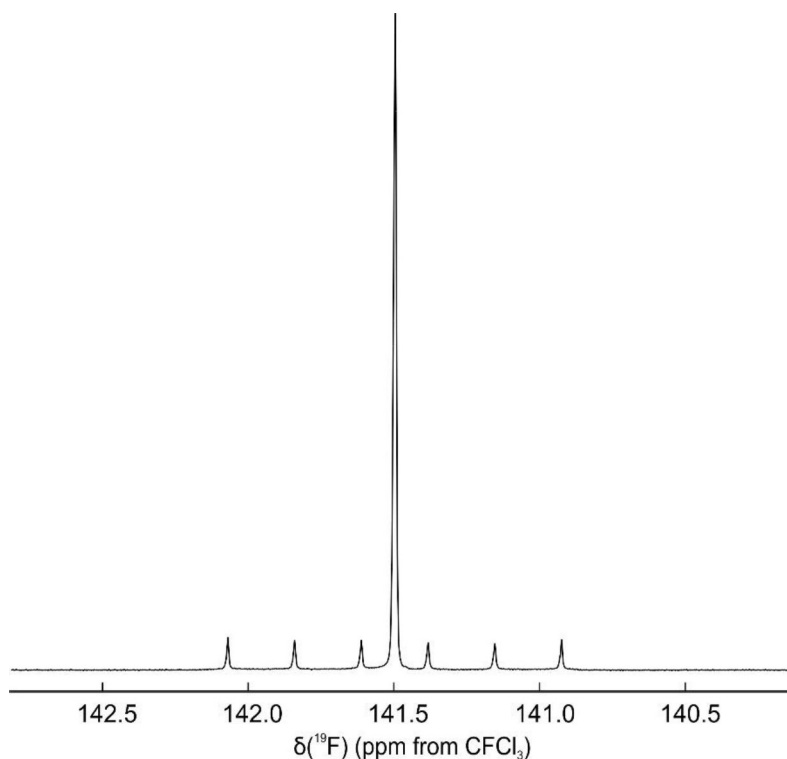
Figure 4. ^{19}F NMR spectrum of $MoOF_4(NC_5H_5)$ in CH_2Cl_2 at room temperature.

Variable-temperature NMR studies were conducted for $MoOF_4(NC_5H_5)_2$ in CH_2Cl_2. Starting at -80 °C, the relative concentration of $MoOF_4(NC_5H_5)_2$ was found to gradually decrease with increasing temperature, and in agreement with the results obtained for the analogous tungsten system,[45] $MoOF_4(NC_5H_5)_2$ is completely dissociated into $MoOF_4(NC_5H_5)$ and C_5H_5N above 0 °C.

Below this temperature, three unique fluorine environments are observed in the ^{19}F NMR spectrum with relative integration values of 2:1:1, and the observed multiplicities correspond to an A_2MX spin system that is expected based on the crystal structure (Figure 5a). At $-80\ °C$, the doublet of doublets at 64.93 ppm is assigned to the two equivalent fluorine atoms in the equatorial plane, and the doublets of triplets at 33.75 ppm and -49.93 ppm are assigned to the equatorial and apical fluorine atoms, respectively, based on the *trans* influence of the Mo=O bond and the analogous assignments previously reported for $WOF_4(NC_5H_5)_2$.[45] In SO_2, decomposition is nearly complete even at $-60\ °C$, consistent with the Lewis-acidic solvent facilitating the dissociation of C_5H_5N.

Interestingly, an additional A_2MX spin system is present in CH_2Cl_2 at $-80\ °C$ ($\delta = 98.46$, 68.64, and -30.71 ppm) (Figure 5b), suggesting that $MoOF_4(NC_5H_5)_2$ also exists in solution as a second isomer (Isomer II) with both pyridyl ligands being adjacent within the equatorial plane. Such a coordination geometry has been previously observed for $WOF_4(L-L)$ adducts with chelating diphosphines (L-L = $Me_2PCH_2CH_2PMe_2$, o-$C_6H_4(PMe_2)_2$),[28] and similar structures have also been proposed for MOF_4(2,2′-bipyridine) (M = Mo, W), WOF_4(1,8-naphthyridine), and WOF_4(2,7-dimethyl-1,8-naphthyridine).[26,46,47] Isomer I was observed as the major component in a dilute CH_2Cl_2 solution at $-80\ °C$ with a molar ratio of 2.4:1 between Isomer I and II.

Confirmation of the plausibility of the proposed isomerization was achieved upon comparison of the relative energies of the two geometry-optimized isomers computed in the gas-phase (DFT-B3LYP). Isomer II was found to be only 10.9 kJ mol^{-1} higher in energy than Isomer I. Isomerism has not been observed for the tungsten congener,[45] which suggests that the formation of Isomer II at low temperatures may be impeded due to the higher Lewis acidity of WOF_4.

a)

Isomer I

F(M)
F(A)
F(A)
F(X)

F(A)

F(M)

F(X)

65.4 65.2 65.0 64.8 64.6   34.3 34.1 33.9 33.7 33.5 33.3   -49.4 -49.6 -49.8 -50.0 -50.2 -50.4

$\delta(^{19}F)$ (ppm from $CFCl_3$)

b)

Isomer II

F(M)
F(M)
F(A)
F(X)

F(A)

F(M)

F(X)

99.4   98.6   97.8   97.0   69.4   69.0   68.6   68.2   67.8   -30.4   -30.8   -31.2

$\delta(^{19}F)$ (ppm from $CFCl_3$)
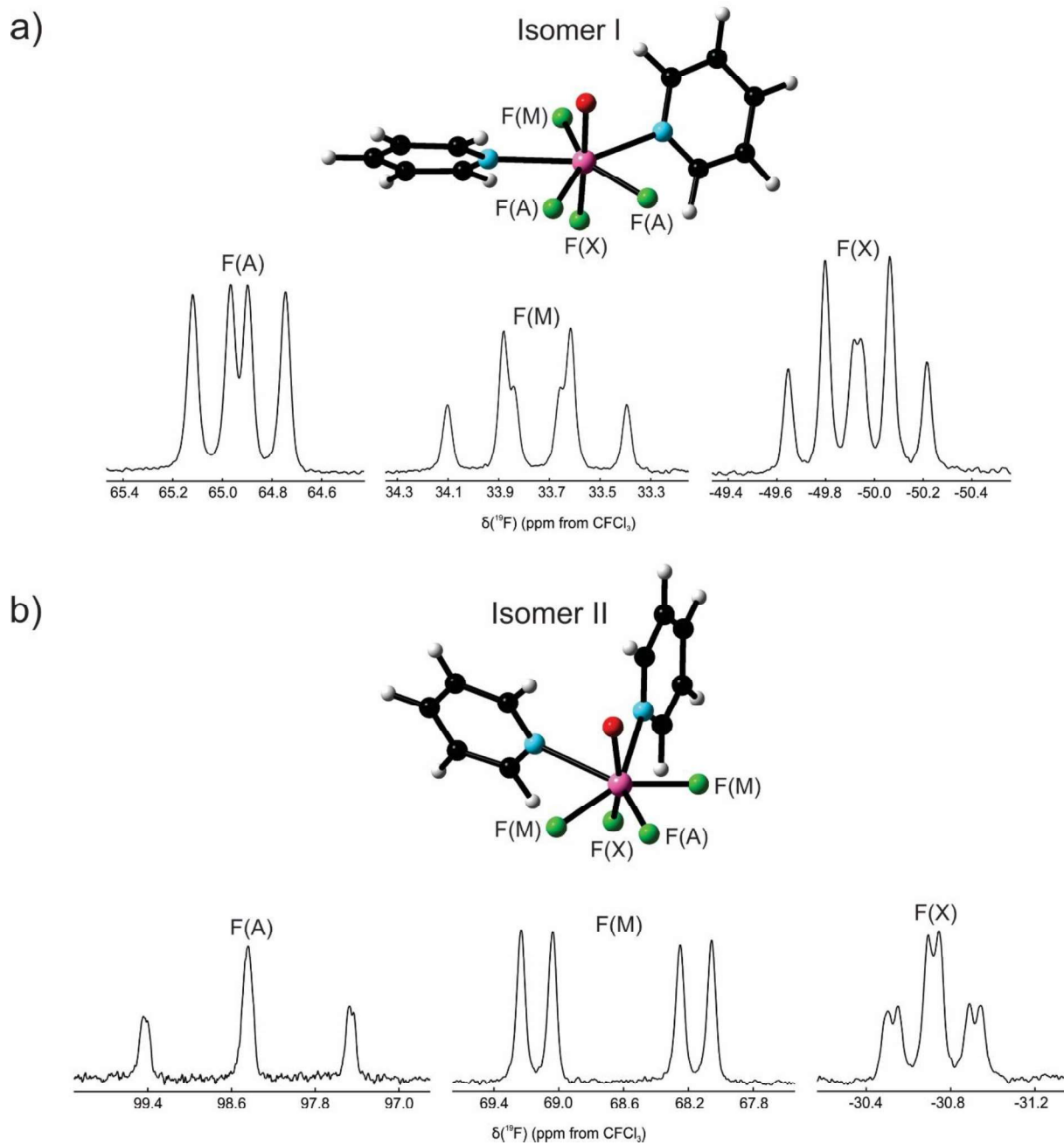
Figure 5. Signals corresponding to a) Isomer I and b) Isomer II in the ^{19}F NMR spectrum of $MoOF_4(NC_5H_5)_2$ in CH_2Cl_2 at –80 °C, along with the optimized gas-phase geometries (DFT-B3LYP).

Comparison of the optimized geometries of the two isomers revealed notable differences in certain structural parameters. The $\angle$(O-Mo-F$_X$) bond angle of Isomer I (calcd.: 169.3°) approaches linearity more closely than that of Isomer II (calcd.: 151.2°) and, while minimal deviation from the least-squares equatorial plane (exptl.: $\leq$ 0.058 Å) is observed for Isomer I, the corresponding plane in Isomer II is quite puckered. In addition, the $\angle$(F$_A$–Mo–F$_M$) and $\angle$(F$_A$–Mo–F$_X$) bond angles for the two isomers differ significantly, and such structural dissimilarities are reflected in the relative magnitudes of their respective $^2J_{FF}$ coupling constants (Table 4). Since the Fermi contact contribution to the $^2J_{FF}$ coupling constant decreases with increasing $\angle$(F–C–F) bond angle,[48] it is not particularly surprising that the magnitudes of the $^2J_{F(A)F(M)}$ coupling constants differ significantly between the two isomers (66 vs. 297 Hz), as the largest structural difference is observed for the $\angle$(F$_A$–Mo–F$_M$) bond angle.

Table 4. ^2J(F,F) coupling constants and bond angles for the two MoOF$_4$(NC$_5$H$_5$)$_2$ isomers.

	Coupling Constant (Hz)			Calculated Bond Angle (°)		
	$^2J_{F(A)F(M)}$	$^2J_{F(A)F(X)}$	$^2J_{F(M)F(X)}$	F(A)–Mo–F(M)	F(A)–Mo–F(X)	F(M)–Mo–F(X)
Isomer I	66	45	80	139.9, 140.6	88.1, 91.9	80.1
Isomer II	297	16	59	76.7, 76.8	110.3	85.1, 85.4

The ^{1}H NMR spectra corroborate this conclusion, as the existence of the second isomer at low temperatures is accompanied by the presence of additional signals in the aromatic region that are of the appropriate relative intensity and multiplicity to correspond to Isomer II. Two different resonances are observed for the *ortho* protons in each isomer due to hindered rotation about the Mo–N bonds because of steric crowding. A detailed discussion of the ^{1}H NMR spectra is provided in the Supporting Information alongside Figure S5.

In addition to the mixture of $MoOF_4(NC_5H_5)_2$ isomers that were observed in the ^{19}F NMR spectrum at –80 °C, an impurity of $[MoOF_5]^-$ was identified by its characteristic doublet (δ = 129.13 ppm) and quintet (δ = –100.09). A singlet was also observed at –44.61 ppm and was tentatively assigned to $MoO_2F_2(NC_5H_5)_2$, which was likely formed due to the presence of trace water. The HF liberated through the formation of $MoO_2F_2(NC_5H_5)_2$ then reacted with $MoOF_4(NC_5H_5)$ to produce $[C_5H_5NH][MoOF_5]$ (eq. (10-12))

$$MoOF_4(NC_5H_5)_2 + H_2O \rightarrow MoO_2F_2(NC_5H_5)_2 + 2HF \qquad (10)$$

$$MoOF_4(NC_5H_5)_2 \rightleftharpoons MoOF_4(NC_5H_5) + C_5H_5N \qquad (11)$$

$$MoOF_4(NC_5H_5) + HF \rightarrow [C_5H_5NH][MoOF_5] \qquad (12)$$
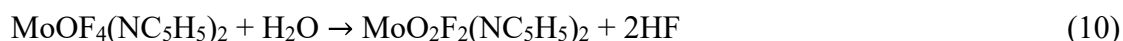
Raman Spectroscopy. Raman spectra were acquired for $MoF_5(NCCH_3)$, $MoF_5(NC_5H_5)_n$ and $MoOF_4(NC_5H_5)_n$ (n = 1, 2), in the solid state at room temperature (Figures 6, S19-20, S22, S24-25), and spectra were also recorded for $MoF_5(NC_5H_5)$ at –100 °C in frozen CH_2Cl_2 or CH_3CN solutions to investigate the nature of the green to orange colour change upon dissolution (Figure S21). Vibrational frequencies were calculated for the (DFT-B3LYP) optimized gas-phase structures and a complete list of experimental and calculated vibrational frequencies and assignments are provided in Tables S19-S24.
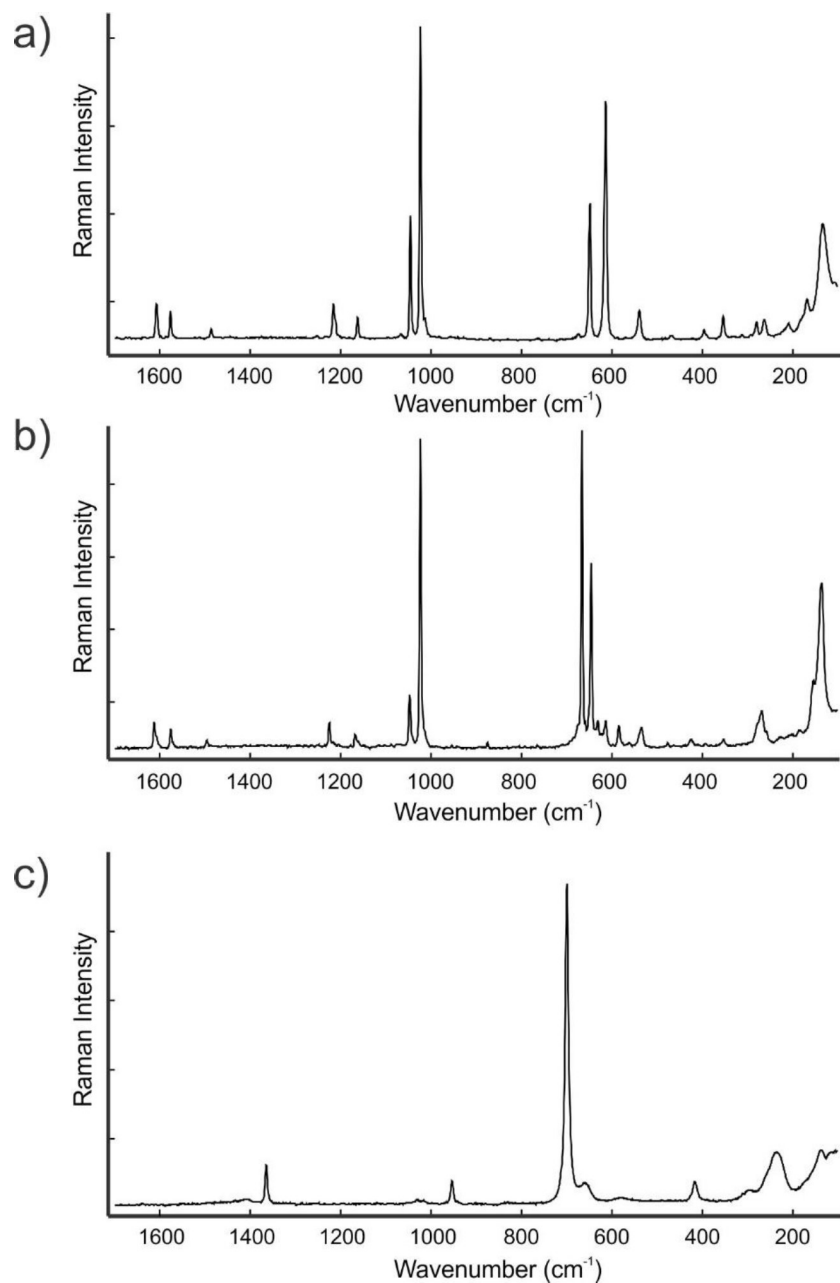
Figure 6. Room-temperature Raman spectra of a) $MoF_5(NC_5H_5)_2$, b) $[MoF_5(NC_5H_5)]_2$, and c) $MoF_5(NCCH_3)$.

The Mo–F stretching modes in $MoF_5(NC_5H_5)_2$ and $MoF_5(NC_5H_5)$ appear at similar frequency ranges with the most intense bands at 649 ($\nu_{as}(MoF_{3,eq})$; calcd.: 641) and 614 cm^{-1} ($\nu_s(MoF_{2,ax}F_{eq})$; calcd.: 615 cm^{-1}) for $MoF_5(NC_5H_5)_2$ and at 666 and 646 cm^{-1} (both $\nu_s(MoF_4)$

coupled with an in-plane deformation mode of C_5H_5N; calcd.: 670 and 649 cm^{-1}) for [MoF$_5$(NC$_5$H$_5$)]$_2$ in the solid state. This is consistent with heptacoordination about molybdenum in both adducts (cf. [MoF$_7$]$^-$: ν_s(MoF$_7$) 686 to 676 cm^{-1}).[35] The Mo–F stretching regions in MoF$_5$(NC$_5$H$_5$)$_n$ are significantly red shifted relative to that of tetrameric MoF$_5$ (757, 736 cm^{-1}),[6] which is expected to possess more covalent terminal Mo–F bonds due to the lower coordination number. Coordination of the pyridyl ligands to the Mo^V centres is corroborated by a consistent and marked blue shift in the symmetric ring-breathing mode (ν_s(NC$_5$)), which appears at 990 cm^{-1} in the spectra of free pyridine[49] and at 1024 cm^{-1} in those for both MoF$_5$(NC$_5$H$_5$)$_n$ adducts. Despite the same frequency for the aforementioned pyridyl modes, the calculated Mo–N stretching modes appear at notably higher frequencies in [MoF$_5$(NC$_5$H$_5$)]$_2$ (calcd.: 182 and 175 cm^{-1}) than in MoF$_5$(NC$_5$H$_5$)$_2$ (calcd.: 137-161 cm^{-1}), consistent with the Mo–N bond lengths in the crystal structures (*vide supra*). The presence of a stronger Mo–N interaction in [MoF$_5$(NC$_5$H$_5$)]$_2$ is attributed to the weak bridging Mo–F bonds, which reduce steric crowding at the metal centre and permit the single Mo–N bond to possess a higher degree of covalency. Based on DFT-B3LYP calculations, the modes of the two pyridyl ligands in MoF$_5$(NC$_5$H$_5$)$_2$ are predicted to be only weakly coupled with a maximal splitting of 3 cm^{-1}; none of these splittings are resolved in the experimental spectrum. In addition, the frequencies of the predominant Mo–F stretching modes in MoF$_5$(NC$_5$H$_5$) do not differ substantially between the solution and solid states, which indicates the absence of a considerable structural change upon dissolution. Indeed, while the most intense Raman band arising from the Mo–F stretching mode of the MoF$_5$(NC$_5$H$_5$) monomer is predicted to appear at 688 cm^{-1}, this signal is not experimentally observed.

In the Raman spectra of MoOF$_4$(NC$_5$H$_5$)$_n$, the ν(Mo=O) modes in MoOF$_4$(NC$_5$H$_5$) (exptl.: 987; calcd.: 1035 cm^{-1}) and MoOF$_4$(NC$_5$H$_5$)$_2$ (exptl.: 957; calcd.:1004 cm^{-1}) are significantly red-

shifted relative to that of $MoOF_4$ (1039 cm^{-1}),[50] consistent with the increase in polarity of the

Mo=O bond upon coordination of the pyridyl ligand(s). As expected, the red shift is more

pronounced in $MoOF_4(NC_5H_5)_2$ due to the higher coordination number. The $\nu(Mo=O)$ mode in

$MoOF_4(NC_5H_5)$ (987 cm^{-1}) is in close agreement with the expected range (ca. 990-1019 cm^{-1})

based on the reported IR data for the hexacoordinate $MoOF_4(L)$ (L = $NCCH_3$, $OP(C_6H_5)_3$,

$OP(CH_3)_3$, $O(CH_2)_4$, $OS(CH_3)_2$, $HCON(CH_3)_2$) adducts.[26] The frequencies of the predominant

symmetric Mo–F stretching bands in the Raman spectra of $MoOF_4(NC_5H_5)$ (exptl.: 678; calcd.:

681 cm^{-1}) and $MoOF_4(NC_5H_5)_2$ (exptl.: 648; calcd.: 657 cm^{-1}) also reflect the difference in

coordination number between the two adducts, with a higher frequency observed for

$MoOF_4(NC_5H_5)$ due to the presence of more covalent Mo–F bonds (cf. $MoOF_4$: $\nu_s(MoF_4)$ 706-716

cm^{-1}).[50] Based on the calculated frequencies for the two isomers of $MoOF_4(NC_5H_5)_2$, no evidence

was found for the presence of Isomer II in the solid state. The strong Mo=O stretching band is

predicted to be very similar (Isomer I: 1004; Isomer II: 999 cm^{-1}) and the experimental band (957

cm^{-1}) did not show any signs of splitting at -100 °C (Figure S23). Similarly, no evidence of a

second isomer in solid $MoF_5(NC_5H_5)_2$ was found.

The frequencies observed in the Raman spectrum of $MoF_5(NCCH_3)$ closely agree with the

literature values, and the presence of a single intense band in the Mo–F stretching region (exptl.:

700; calcd.: 704 cm^{-1}; lit.: 697 (Raman) or 703 cm^{-1}(IR))[15,22] is a testament to sample purity. In

addition, the $\nu_s(CN)$ mode of CH_3CN (2297 cm^{-1}) is significantly blue-shifted relative to that of

free CH_3CN (2253 cm^{-1}), which confirms the coordination of the organic ligand.

EPR Spectroscopy. EPR spectra were recorded for $MoF_5(NCCH_3)$, $[MoF_5(NC_5H_5)]_2$, and

$MoF_5(NC_5H_5)_2$ as microcrystalline powders dispersed in finely-ground solid adamantane (ca. 1 wt.

%). No signals were present in the room-temperature EPR spectrum of $MoF_5(NCCH_3)$, other than

an isotropic signal that is consistently observed for FEP once it has been passivated with elemental F_2 (*vide infra*). In addition, the EPR spectrum of $[MoF_5(NC_5H_5)]_2$ contained only a weak rhombic signal at room temperature. Based on DFT-B3LYP calculations in the gas phase, $[MoF_5(NC_5H_5)]_2$ is predicted to be significantly more stable in the triplet state than in the singlet state, with an energy difference of 108.9 kJ mol^{-1} separating the two spin configurations. Nevertheless, the observed signal was attributed to a trace impurity of $MoF_5(NC_5H_5)_2$ due to the close resemblance of the rhombic trace to the intense signal observed in the EPR spectrum of the 1:2 adduct (*vide infra*).

Variable-temperature EPR studies were performed for $MoF_5(NC_5H_5)_2$ dispersed in adamantane and EPR parameters were computed using DFT methods within the ORCA software package using GGA functionals (BPW91 and PBE) on both the gas-phase optimized structure (DFT-B3LYP) and the crystal structure geometry (Tables 5 and S25) to assist in the interpretation of the experimental spectra. While axial patterns were observed for $[MoOF_4]^-$ and $[MoOF_5]^{2-}$ in single-crystal and frozen-glass EPR spectra,[16,17,51] the lower C_2 molecular symmetry of $MoF_5(NC_5H_5)_2$ is associated with a higher degree of anisotropy, resulting in a recognizably rhombic signal even at room temperature that sharpens significantly on cooling to give a distinct rhombic powder pattern well before reaching the lowest measured temperature of $-155\ °C$ (Figures 7 and S27). The spin density isosurface of $MoF_5(NC_5H_5)_2$ (Figure 8) indicates that the d^1 electron is largely localized on the molybdenum centre, although significant electron density is also present on the axial and symmetry equivalent equatorial fluorido ligands. The complete absence of hyperfine splitting even at $-155\ °C$ is strongly suggestive of relaxation due to inter-electron dipolar coupling between paramagnetic centres in neighbouring unit cells within microcrystalline $MoF_5(NC_5H_5)_2$ particles; however, the dispersion of those particles in the adamantane powder is

evidently sufficiently random to yield an undistorted powder spectrum. The generalized line broadening observed at higher temperatures (up to, but not beyond, room temperature) can therefore be attributed, as usual, to spin-orbit coupling (SOC).
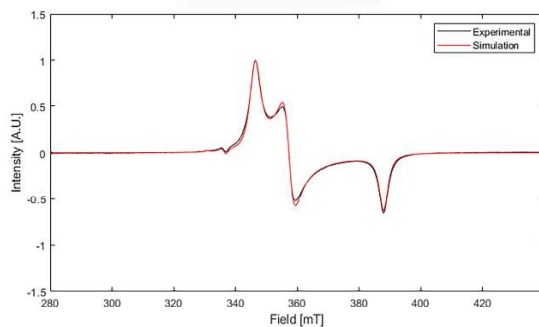
Figure 7. Experimental and simulated rhombic EPR spectra of microcrystalline $MoF_5(NC_5H_5)_2$ (1.7 wt. %) dispersed in powdered adamantane at $-155\ °C$ in a ¼ in. o.d. FEP reactor. The small axial feature at 330-340 mT is caused by F_2 passivation of the reactor.
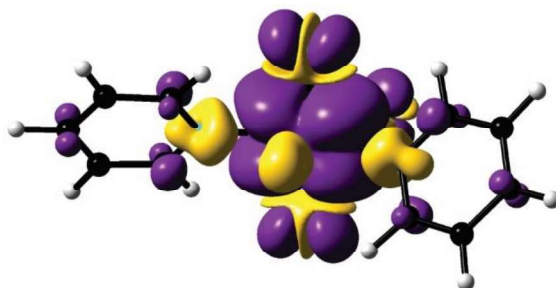
Figure 8. Spin density isosurface of $MoF_5(NC_5H_5)_2$, computed from the optimized gas-phase geometry (DFT-B3LYP). Isosurface values are drawn at $0.0004\ e\ Å^{-3}$.

Table 5. Simulated and calculated EPR spectral parameters for MoF$_5$(NC$_5$H$_5$)$_2$ dispersed in powdered adamantane at −155 °C.^{a}

	FEP Sim.	MoF$_5$(NC$_5$H$_5$)$_2$		
		Sim.	Calcd.^{b}	
			Optimized Geometry	X-Ray Structure
g_{iso}	2.0171^c	1.8590	1.9079	1.9164
g_x^{d}	2.0053	1.9486	1.9807	1.9817
g_y^{d}	2.0053	1.8887	1.9237	1.9402
g_z^{d}	2.0406	1.7396	1.8194	1.8273
lw [mT]^e	0.947	3.581		
lw% lor^f	26.2	83.4		
Γ_x [MHz]^g	42.719	50.258		
Γ_y [MHz]^g	67.338	52.367		
Γ_z [MHz]^g	42.379	14.624		

^{a} The MoF$_5$(NC$_5$H$_5$)$_2$ signal was refined to a weight of ca. 1000:1 with respect to the FEP signal. ^{b} Calculated using ZORA at the BPW91 level of theory with the IGLO-III basis sets (H, C, N, F) and the segmented all-electron relativistically contracted (SARC) basis set (Mo).[52] Optimized geometry at the B3LYP/aVTZ level of theory – see Table 2. X-ray geometry: CIF converted to Cartesian coordinates and symmetrized to C_2.^{c} Experimental g_{iso} = 2.0155 at 22 °C. ^{d} EPR coordinates for axial system defined such that g_z is the unique value ($g_\parallel$) and $g_{x,y}$ identical ($g_\perp$); for rhombic system such that g_z is most widely separated from the other two and g_y is the intermediate value.[53] ^{e} Linewidths correspond to isotropic full-width-at-half-maximum values.^{f} % of Lorentzian character; balance is Gaussian. ^{g} Anisotropic full width at half maximum broadening values (100 % Gaussian).

In the course of the present study, we determined that an EPR signal attributed to FEP is induced by the F$_2$ passivation process, as FEP reactors did not give rise to an EPR signal prior to treatment with elemental F$_2$. The FEP signal manifested as a sharp singlet at room temperature (g_{iso} = 2.0155), although it broadened significantly at −30 °C and converted to an axial powder pattern on reaching −155 °C (Figure 7), most likely due to reduced molecular motion within the plastic at low temperatures. While signals corresponding to FEP radicals have been previously reported,[54–57] the nature of defect signals in the passivated reactor is of fundamental interest.

Further discussion of the FEP defect caused by F_2 passivation is presented in the Supporting Information alongside Figure S26.

The *g*-tensors computed for the X-ray and gas-phase optimized geometries (Table 6) differ only negligibly. Since EPR parameters are known to change dramatically with only slight modifications in molecular geometry,[18] the close agreement between the experimental and calculated g-tensor components indicates that the $MoF_5(NC_5H_5)_2$ adduct most likely exists as a single isomer in the solid state. The absence of isomerization is corroborated by the large energy difference (55.6 kJ mol^{-1}) computed between the two optimized structures for Isomer I and II (DFT/B3LYP) in the gas phase (Figures S6-7). The equivalent $g_{iso} = 1.8590$ is less than $g_e = 2.0024$; this is in accordance with the expectation that for a d^{1-5} electron configuration, $g < g_e$.[58]
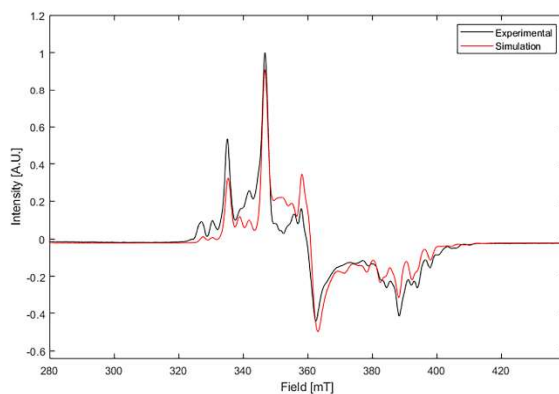
Figure 9. Experimental and simulated EPR spectra of microcrystalline $MoF_5(NC_5H_5)_2$ (0.93 wt. %) dispersed in a $MoOF_4(NC_5H_5)_2$ matrix in a ¼ in. o.d. FEP reactor at −155 °C.

Table 6. Simulated EPR spectral parameters for MoF₅(NC₅H₅)₂ in MoOF₄(NC₅H₅)₂ at –155 °C, as well as calculated values determined from the gas-phase optimized geometry.

	Sim.[a]			Calcd.[b]		
	x^c	y^c	z^c	x^c	y^c	z^c
g	1.945	1.890	1.737	1.981	1.924	1.819
A (Mo) [MHz]	82.1	–144.6	160.7 8	53.2	–193.4	103.8
A (F₁) [MHz][d]	—	—	—	–16.8	–1.7	–0.1
A (2 F₂) [MHz][d]	310.5	–108.9	97.1	331.6	–184.7	59.6
A (2 F₃) [MHz][d]	–6.3	–34.8	140.6	–8.7	–34.1	139.1
Γ [MHz][e]	8.0	31.5	0.000	—	—	—

[a] lw [mT] = 2.072; line shape (% Lorentzian) = 18.6. [b] Calculated using ZORA at the BPW91 level of theory with the IGLO-III basis sets (H, C, N, F) and the segmented all-electron relativistically contracted (SARC) basis set (Mo), and fitted to the simulation framework employed in EasySpin.[52] Optimized geometry at the B3LYP/aVTZ level of theory – see Table 2. [c] EPR coordinates for rhombic system defined such that g_z is most widely separated from the other two and g_y is the intermediate value.[53] [d] Numbering scheme is consistent with the labelling in Figure 1a. [e] Anisotropic full width at half maximum broadening values (100 % Gaussian).

Computations predict that the A-tensor of MoF₅(NC₅H₅)₂ is dominated by the two pairs of symmetry equivalent fluorine nuclei with significant spin density (i.e. F(2) and F(3) in Figure 1a) and Mo, with only minor contributions associated with the remaining F, C, N and H nuclei (Table 6). The isomorphous crystal structures of MoOF₄(NC₅H₅)₂ and MoF₅(NC₅H₅)₂ afforded an opportunity to characterize the EPR spectrum of MoF₅(NC₅H₅)₂ as a dilute solid solution dispersed within the crystal lattice of the diamagnetic MoOF₄(NC₅H₅)₂ host, thus minimizing dipolar line broadening so as to resolve at least some of the hyperfine coupling. In order to incorporate MoF₅(NC₅H₅)₂ into the MoOF₄(NC₅H₅)₂ lattice, the two adducts were prepared simultaneously by

distilling an excess of C_5H_5N on top of a mixture of MoF_5 and $MoOF_4$. The resulting suspension was vigorously sonicated and removal of the volatile materials afforded a faint pink polycrystalline mixture.

Similar to the spectra recorded in the adamantane matrix, a rhombic signal was observed. In addition, a partially resolved hyperfine structure was present in the room-temperature spectrum and further splitting was observed upon cooling the sample to -155 °C (Figure 9). The g-values for $MoF_5(NC_5H_5)_2$ measured in the matrix at low temperature are close to those determined for $MoF_5(NC_5H_5)_2$ in adamantane, and the presence of additional fine structure enabled the determination of the A-tensor components for select nuclei (Table 7). Only inclusion of hyperfine coupling to the axial and symmetry-equivalent equatorial fluorido ligands (^{19}F, $I = 1/2$, 100 %) and the $^{95/97}Mo$ isotopes ($I = 5/2$, 25 %) was required to accurately simulate the experimental spectra. The Mo satellites are most evident in the two small peaks at 325 and 330 mT (Figure 9). Nevertheless, unresolved hyperfine coupling from the remaining high-abundance isotopes, i.e., the unique ^{19}F, two ^{14}N, and ten ^1H nuclei, contribute to the overall line broadening, as reflected in a predominantly Gaussian line shape. The presence of unresolved hyperfine structure is not particularly surprising, as previously reported EPR spectra of even relatively simple Mo^V systems, such as powdered samples of $[MoOF_4]^-$ and supercooled solutions of $[MoOF_5]^{2-}$,[16,17,51] have suffered from insufficient resolution and have thus been deemed too complex to permit comprehensive analysis.

Relatively poor fitting of the simulation to the experimental trace occurs in the central (g_y) region of the spectrum. Interestingly, multiple spectra recorded at -155 °C, and at both slightly higher and at cryogenic temperatures (-263 °C) revealed significant modifications in the EPR signal between subsequent scans (Figure S27), which particularly affected the central region,

indicating that the sample is fluxional at low temperatures. Although a chemical change was initially suspected, such as oxidation of the guest by the host material, rewarming the sample to room temperature gave rise to the same signal that was observed prior to cooling. Such line-shape distortion effects are most likely attributable to the partial ordering of crystallites in the loosely packed powder sample in the presence of an external magnetic field (additional discussion is provided in Supporting Information alongside Figure S27).[59] This conclusion is supported by the observation of more pronounced fluctuations at low temperatures, in accordance with Curie's law.[59] In an attempt to observe additional fine structure, EPR measurements were also conducted on the doped sample in liquid helium at -263 °C in a quartz tube. No further reductions in spectral line width were observed compared to -155 °C, indicating that SOC-derived line broadening is already fully quenched at the higher temperature.

Molecular Orbitals, Dimerization Energy Calculations, and NBO Analyses. Frontier orbital energies and corresponding absorption wavelengths are provided in Table S26. NPA charges and Wiberg valences for all atoms are compiled in Table S27, and NPA charges and Wiberg bond indices (WBIs) are presented in Tables 7 and S28.

Similar to monomeric MoF_5 (C_s),[6] the SOMOs and LUMOs of the MoF_5 adducts are dominated by π^* Mo(d)–F(p) interactions, with negligible electron density localized on the organic moieties. In triplet $[MoF_5(NC_5H_5)]_2$, the SOMO 1 possesses additional antibonding interactions between the Mo centres and the bridging fluorido ligands, whereas the SOMO 2 is non-bonding between these atoms (Figure 10). The SOMO–1 and SOMO–2 of $MoF_5(NC_5H_5)_2$ and $[MoF_5(NC_5H_5)]_2$ are both localized on the pyridyl moieties, rendering the SOMO–1 to SOMO transitions ligand-to-metal charge-transfer (LMCT) transitions, which are predicted to be lower in energy than the corresponding SOMO-LUMO (d-d) transitions. The SOMO–1 of $MoF_5(NCCH_3)$,

on the other hand, is primarily centered on the fluorido ligands. Additionally, the calculated N≡C bond lengths of $MoF_5(NCCH_3)$ (1.143 Å) and uncoordinated CH_3CN (1.150 Å) are very similar, which is consistent with the weak π-accepting ability of this ligand.

The HOMO-LUMO transitions in $MoOF_4(NC_5H_5)_n$ ($n = 1, 2$) are identified as LMCT transitions, with predicted absorption energies within the UV region. The LUMOs of $MoOF_4(NC_5H_5)$ and $MoOF_4(NC_5H_5)_2$ consist of π^* $Mo(d_{xy})$–$F(p_{x/y})$ interactions, with that of the latter adduct being comparable to the SOMO found in $MoF_5(NC_5H_5)_2$ (Figure 11).

SOMO–1 (–8.38 eV)   SOMO 2 (–6.87 eV)

SOMO 1 (–6.55 eV)   LUMO (–3.67 eV)
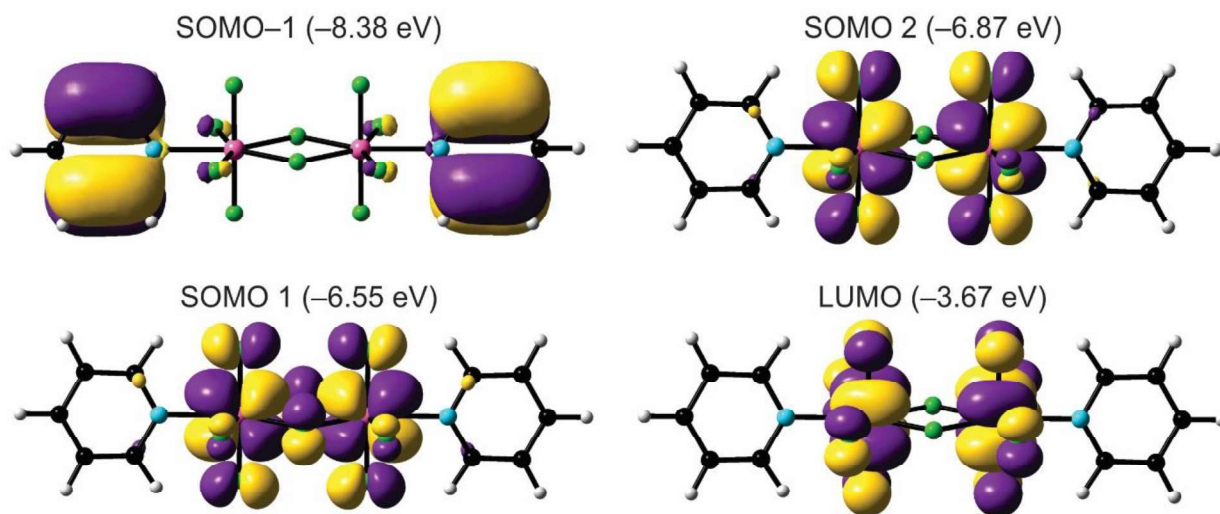
Figure 10. Frontier MOs (DFT-B3LYP) of $[MoF_5(NC_5H_5)]_2$ in the triplet state. Isosurface values are drawn at 0.02 e Å^{-3}.
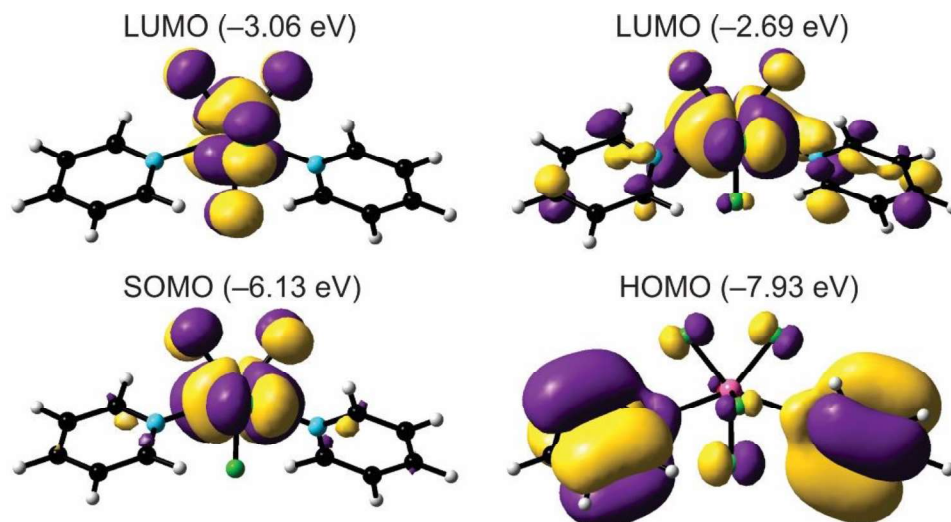
Figure 11. Frontier MOs (DFT-B3LYP) of $MoF_5(NC_5H_5)_2$ (left) and $MoOF_4(NC_5H_5)_2$ (right). Isosurface values are drawn at 0.02 e $Å^{-3}$.

Since the LUMO of monomeric, C_{4v}-symmetric $MoOF_4$ is dominated by $\pi^*(Mo(d_{xy})-F(p_{x/y}))$ interactions, this orbital does not possess the appropriate symmetry to interact with incoming σ-donors along the C_4 axis. In contrast, the LUMO+3 (−1.90 eV) contains a significant contribution from the d_{z^2} orbital on molybdenum, which facilitates the coordination of C_5H_5N *trans* to the M=O bond. According to second-order perturbation theory analysis, the principal N→Mo donor-acceptor interaction in $MoOF_4(NC_5H_5)$ (192.5 kJ mol^{-1}) involves $\sigma(Mo-N)$ and $\sigma^*(Mo=O)$ orbital contributions, which is consistent with the elongation of the Mo=O bond upon adduct formation. Although the population of a $\sigma^*(Mo=O)$ orbital is also observed in the case of $MoOF_4(NC_5H_5)_2$, the corresponding N→Mo donor-acceptor interaction is less pronounced (25.1 kJ mol^{-1}), which reflects the change in geometry and the significance of steric crowding in reducing the Mo=O bond order in the heptacoordinate species.

To investigate why dimerization is observed for $MoF_5(NC_5H_5)$, but not for $MoOF_4(NC_5H_5)$, the counterpoise-corrected binding energies (dimerization energies) for both adducts were computed in the gas phase (eq. (13-14)).[60]

$$2MoF_5(NC_5H_5) \rightarrow [MoF_5(NC_5H_5)]_2 \tag{13}$$

$$2MoOF_4(NC_5H_5) \rightarrow [MoOF_4(NC_5H_5)]_2 \tag{14}$$

Two potential dimers were investigated for $[MoOF_4(NC_5H_5)]_2$, the first of which contained both oxido ligands in the *syn* configuration (approximate C_s symmetry), while the second approximated C_i symmetry (*anti* oxido ligand configuration) (Figure 12). Although the dimerization of $MoF_5(NC_5H_5)$ and $MoOF_4(NC_5H_5)$ are both endothermic processes, the dimerization energy of $[MoF_5(NC_5H_5)]_2$ (21.6 kJ mol^{-1}) is significantly lower than that of $[MoOF_4(NC_5H_5)]_2$ (130.4 kJ mol^{-1} for C_i dimer, 132.6 kJ mol^{-1} for C_s dimer), which is indicative of a higher probability of formation.
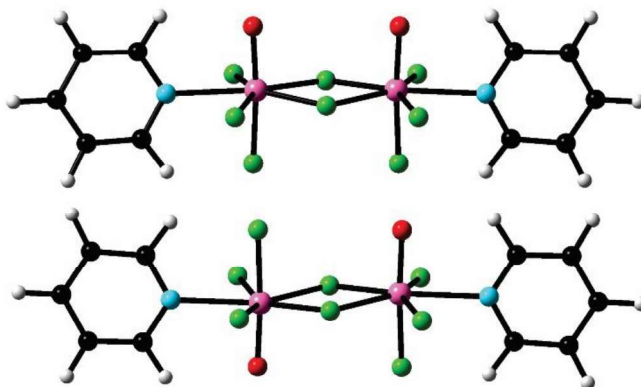
Figure 12. Optimized gas-phase geometries (DFT-B3LYP) of the *syn* (top) and *anti* (bottom) isomers considered for $[MoOF_4(NC_5H_5)]_2$.

Table 7. Selected NPA Charges and WBIs of MoF$_5$(NCCH$_3$), MoF$_5$(NC$_5$H$_5$)$_n$, and MoOF$_4$(NC$_5$H$_5$)$_n$ (n = 1, 2), as well as the corresponding values for monomeric MoF$_5$ (C_s) and MoOF$_4$ (C_{4v}).

Species	Mo Charge	N Charge	Sum of Charges on Base	WBI Mo–F	Mo–N	Mo–O
MoF$_5$	+2.36	—	—	0.72–0.85	—	—
[MoF$_5$(NC$_5$H$_5$)]$_2$[a]	+2.17	–0.43	+0.30	F$_t$: 0.72, 0.78	0.44	—
				F$_b$: 0.37		
MoF$_5$(NC$_5$H$_5$)$_2$	+2.11	–0.43	+0.26	0.67–0.71	0.38	—
MoF$_5$(NCCH$_3$)	+2.22	–0.40	+0.18	0.71–0.81	0.31	—
MoOF$_4$	+2.30	—	—	0.75	—	1.97
MoOF$_4$(NC$_5$H$_5$)	+2.21	–0.52	+0.13	0.72	0.18	1.97
MoOF$_4$(NC$_5$H$_5$)$_2$ Isomer I	+2.06	–0.42	+0.28	0.55–0.68	0.38	1.90
MoOF$_4$(NC$_5$H$_5$)$_2$ Isomer II	+2.13	–0.43	+0.23	0.54–0.74	0.32	1.82

[a] Values correspond to triplet state.

As expected, the charge on the Mo$^{V/VI}$ centre decreases upon adduct formation, with a slightly greater charge reduction observed upon coordination of two organic bases as opposed to one. Comparison of the WBIs for the MoF$_5$ and MoOF$_4$ adducts reveals significant variation in the strength of the dative Mo–N bond. According to Table 7, the Mo–N bonds in [MoF$_5$(NC$_5$H$_5$)]$_2$ possess the greatest degree of covalent character (WBI of 0.44) due to the presence of highly ionic 3c-4e$^-$ Mo–F–Mo bonds that reduce steric congestion in the pentagonal bipyramidal coordination sphere. Similarly, the Mo–N bonds in MoF$_5$(NC$_5$H$_5$)$_2$ (WBI of 0.38) and MoOF$_4$(NC$_5$H$_5$)$_2$ (WBIs of 0.38 and 0.32 for Isomer I and II, respectively) also possess a high degree of covalency, although the Mo–N bond in the second MoOF$_4$(NC$_5$H$_5$)$_2$ isomer is slightly weaker due to more significant steric crowding when the pyridyl ligands occupy adjacent coordination sites. In contrast, the Mo–N bond in MoOF$_4$(NC$_5$H$_5$) (WBI of 0.18) possesses the lowest degree of covalent character due to

the strong *trans* influence exerted by the oxido ligand. Whereas the strengths of the Mo–N bonds are greater than one-third of the Mo–F bonds in $MoF_5(NC_5H_5)_2$, $MoF_5(NCCH_3)$, and $MoOF_4(NC_5H_5)_2$, the Mo–N bond strength is just one-quarter of that of the Mo–F bonds for $MoOF_4(NC_5H_5)$. Consistent with this observation, the pyridyl ligand in $MoOF_4(NC_5H_5)$ donates a significantly smaller charge (+0.13) than those in $MoF_5(NC_5H_5)_n$ and $MoOF_4(NC_5H_5)_2$ (+0.23 to +0.30).

In agreement with the observed red shifts in the Mo–F vibrational frequencies, adduct formation is accompanied by an elongation of the Mo–F bonds, with more pronounced effects associated with the heptacoordinate species due to the higher coordination number. Although only marginal reductions in the WBIs of the Mo–F bonds are observed for $MoF_5(NCCH_3)$ and $MoOF_4(NC_5H_5)$, the strengths of the Mo–F bonds in $[MoF_5(NC_5H_5)]_2$ vary remarkably, with the terminal and axial bonds (WBIs of 0.78 and 0.72, respectively) possessing significantly greater covalent character than the bridging bonds (WBI of 0.37). In fact, the WBI of the bridging Mo–F bonds is even lower than the WBI of the corresponding Mo–N bond (0.44), which corroborates the high ionicity of the bridging bonds.

CONCLUSIONS

For the first time, adducts of MoF_5 with organic bases were conclusively characterized. While only the 1:1 adduct with CH_3CN, $MoF_5(NCCH_3)$, could be isolated, two adducts with C_5H_5N were identified, i.e., $MoF_5(NC_5H_5)_n$ (n = 1, 2). Single-crystal X-ray diffraction revealed that $MoF_5(NC_5H_5)_2$ adopts a pentagonal-bipyramidal geometry, whereas the 1:1 adduct was found to exist in the dimeric $[MoF_5(NC_5H_5)]_2$ form in the solid state. For comparison, the $MoOF_4(NC_5H_5)_n$ (n = 1, 2) adducts were also synthesized and structurally characterized by X-ray

crystallography. While $MoF_5(NC_5H_5)_2$ and $MoOF_4(NC_5H_5)_2$ are isomorphous, fundamental differences in the Lewis-acid behaviour of MoF_5 and $MoOF_4$ were observed upon reaction with one equivalent of C_5H_5N, as evidenced by the formation of $[MoF_5(NC_5H_5)]_2$ and $MoOF_4(NC_5H_5)$, respectively. Low-temperature multinuclear NMR spectroscopy revealed an unprecedented isomerism of the $MoOF_4(NC_5H_5)_2$ adduct in solution with the pyridyl ligands occupying non-adjacent or adjacent coordination sites in the pentagonal plane at low temperatures. The EPR spectra of $MoF_5(NC_5H_5)_2$ as a microcrystalline powder dispersed in adamantane showed a distinct rhombic pattern that is in very good agreement with g-tensor calculations at the DFT level using GGA-ZORA approaches employing relativistic all-electron wavefunctions for Mo.[52] These results provide strong support for the Mo^V oxidation state with spin density concentrated at Mo. Spectra obtained from the Mo^V centre dispersed in an isomorphous Mo^{VI} host are complex; however the dominant ^{19}F and $^{95/97}Mo$ hyperfine splittings were obtained from spectral simulations with the help of these computational approaches. Calculations at the DFT/B3LYP level of theory coupled with NBO analyses further elucidate the distinctive bonding and structural properties of the adducts, and computed dimerization energies of $MoF_5(NC_5H_5)$ and $MoOF_4(NC_5H_5)$ explain why dimerization is observed for the former complex only.

EXPERIMENTAL SECTION

Caution! Anhydrous HF and MoF$_6$ are highly toxic and corrosive, and condensing MoF$_6$ on top of silicon powder in the absence of solvent may result in detonation.[31]

Materials and Apparatus. All reactions were performed in heat-sealed ¼ in. o.d. tetrafluoroethene-hexafluoropropene copolymer (FEP) reactors that were connected to stainless-steel valves via flared fittings and passivated with 100 % F_2. Volatile materials were distilled on a

Pyrex vacuum line equipped with glass valves fitted with 6-mm-o.d. PTFE stopcocks (J. Young), with the exceptions of MoF_6 and aHF, which were distilled through a nickel/316 stainless-steel vacuum line equipped with 316 stainless-steel valves (Autoclave Engineers) and prepassivated with 100 % F_2. Solid materials were handled in a drybox (Omni Lab, Vacuum Atmospheres) under an atmosphere of dry N_2.

Acetonitrile (Baker, 99.8%) was dried as described previously,[61] and pyridine (Sigma-Aldrich, 99.8%) was dried over CaH_2 and distilled prior to use. Dichloromethane was distilled from a solvent purification system (M. Braun MB-SPS) onto 4 Å molecular sieves and distilled once more onto fresh sieves. Molybdenum hexafluoride (Ozark-Mahoning) was distilled prior to use. $MoOF_4$ was prepared according to a literature procedure.[62]

Syntheses. *MoF₅.* MoF_5 was prepared as reported previously.[31] In the dry box, a ¼ in. o.d. FEP reactor was loaded with silicon powder (0.0127 g, 0.452 mmol). Anhydrous HF (0.674 g) was distilled into the reactor at −196 °C, followed by MoF_6 (0.567 g, 2.70 mmol). The reactor was warmed to room temperature, yielding a bright yellow oil that formed over 30 min. Upon briefly submerging the reactor in liquid nitrogen, the yellow oil was converted into a fine yellow powder, which persisted even when the reactor was rewarmed to room temperature. The volatile materials were then removed under dynamic vacuum, affording MoF_5 (0.305 g, 1.60 mmol, 88.3 % yield with respect to silicon) as a light yellow powder.

In a second synthesis, a ¼ in. o.d. FEP reactor was loaded with tungsten powder (0.0283 g, 0.154 mmol). Following the addition of anhydrous HF (0.460 g) and MoF_6 (0.382 g, 1.82 mmol) at −196 °C, the reactor was warmed to −70 °C and was vigorously agitated and sonicated to afford a viscous yellow oil. The reaction was allowed to stand at room temperature for 16 h, and the reactor was then briefly frozen in liquid nitrogen to convert the yellow oil into a pale yellow

powder. The volatile materials were removed at −80 °C for 2 h and at room temperature for 2 h to afford MoF$_5$ as a fine yellow powder (0.176 g, 0.922 mmol, 99.8 % yield with respect to tungsten).

MoF$_5$(NC$_5$H$_5$)$_2$. In the dry box, a ¼ in. o.d. FEP reactor was loaded with MoF$_5$ (0.0189 g, 0.0990 mmol). Pyridine (0.668 g, 8.45 mmol) was then distilled into the reactor at −196 °C. Upon warming to −40 °C and gently agitating the reactor, a light pink powder immediately precipitated from solution. The reactor was briefly sonicated to ensure reaction completion. The volatile materials were subsequently removed under dynamic vacuum at −25 °C for 30 min and at room temperature for 10 min to afford MoF$_5$(NC$_5$H$_5$)$_2$ as a pale pink powder (0.035 g, 0.10 mmol, expected 0.0346 g). A trace impurity of [MoOF$_5$]$^-$ (δ =129.82 ppm (d), −102.46 ppm (s, br)) was identified via ^{19}F NMR spectroscopy (CH$_2$Cl$_2$, 300 MHz, −80 °C, unlocked).

In a second synthesis, a ¼ in. o.d. FEP reactor was loaded with MoF$_5$ (0.0408 g, 0.214 mmol). Dichloromethane (0.575 g) and pyridine (0.034 g, 0.43 mmol) were subsequently distilled into the reactor at −196 °C, and a light pink suspension formed upon gentle agitation and sonication at −85 °C. The volatile materials were removed under dynamic vacuum at −50 °C for 3 h and at room temperature for 30 min to afford MoF$_5$(NC$_5$H$_5$)$_2$ as a pale pink powder (0.074 g, 0.21 mmol, 99 % with respect to MoF$_5$).

[MoF$_5$(NC$_5$H$_5$)]$_2$. In the dry box, a ¼ in. o.d. FEP reactor was loaded with MoF$_5$ (0.0560 g, 0.293 mmol). Dichloromethane (9.05 g) was distilled into the reactor at −196 °C, followed by pyridine (0.022 g, 0.28 mmol). Warming the reactor to −90 °C afforded a dark purple solution, which was quickly converted into a bright orange solution upon gentle agitation. The reactor was briefly sonicated and then kept at −85 °C for 1 h, although no indication of further reaction was evident. The volatile materials were removed under dynamic vacuum at −60 °C for 1.5 h and at room temperature 2 h, affording [MoF$_5$(NC$_5$H$_5$)]$_2$ as a green powder (0.073 g, 0.14 mmol, 97 % with

respect to pyridine). Three weak singlets likely corresponding to trace Mo^{VI} impurities ($\delta = 141.73$ ppm, 142.66 ppm ($MoOF_4(NC_5H_5)$), and 188.98 ppm) were observed via ^{19}F NMR spectroscopy (CH_2Cl_2, 300 MHz, room temperature, unlocked).

$MoOF_4(NC_5H_5)_2$. In the dry box, a ¼ in. o.d. FEP reactor was loaded with $MoOF_4$ (0.031 g, 0.16 mmol). Pyridine (0.668 g, 8.45 mmol) was then distilled into the reactor at $-196\ ^\circ C$. Warming the reactor to $-35\ ^\circ C$ afforded a white suspension that contained traces of a light green material. The reactor was vigorously agitated and sonicated to ensure reaction competition, during which the green colour disappeared. The volatile materials were then removed at $-30\ ^\circ C$ for 1 h and at room temperature for 15 min to afford $MoOF_4(NC_5H_5)_2$ as a fine white powder (0.057 g, 0.16 mmol, 100 % yield with respect to $MoOF_4$). NMR (ppm, CH_2Cl_2, 300 MHz, $-80\ ^\circ C$, unlocked): ^{19}F 140.88 (s, $MoOF_4(NC_5H_5)$); 98.46 (td, F(A) Isomer II, $^2J(F(A)-F(M)) = 297$ Hz, $^2J(F(A)-F(X)) = 16$ Hz); 68.64 (dd, F(M) Isomer II, $^2J(F(M)-F(X)) = 59$ Hz); 64.93 (dd, F(A) Isomer I, $^2J(F(A)-F(M)) = 66$ Hz, $^2J(F(A)-F(X)) = 45$ Hz); 33.75 (dt, F(M) Isomer I, $^2J(F(M)-F(X)) = 80$ Hz); -30.71 (td, F(X) Isomer II); -49.93 (dt, F(X) Isomer I). Impurities of $[MoOF_5]^-$ ($\delta = 129.13$ ppm (d), -100.09 ppm (br)) and $MoO_2F_2(NC_5H_5)_2$ ($\delta = -44.61$ ppm, (s)) were identified by ^{19}F NMR spectroscopy. ^1H 3.91 (s, CH_2Cl_2); 6.24 (m, H_m Isomer I), 6.66 (t, H_p Isomer I, $^3J(H_p-H_m) = 7.5$ Hz); 7.17 (s, H_{o1}, Isomer I); 7.60 (s, H_{o2}, Isomer I); 6.11 (m, H_m Isomer II), 6.53 (t, H_p Isomer II, $^3J(H_p-H_m) = 7.5$ Hz); 7.48 (d, H_{o1}, Isomer II, $^3J(H_o-H_m) = 4.5$ Hz); 7.58 (s, H_{o2}, Isomer II); Impurity of $[C_5H_5NH]^+$ (14.75, s; other resonances overlapping with adducts).

$MoOF_4(NC_5H_5)$. In the dry box, a ¼ in. o.d. FEP reactor was loaded with $MoOF_4$ (0.0267 g, 0.142 mmol). Dichloromethane (0.512 g) was then distilled into the reactor at $-196\ ^\circ C$, followed by pyridine (0.012 g, 0.152 mmol). The reactor was warmed to $-75\ ^\circ C$ to afford a white suspension, which dissolved upon gentle agitation to afford a colourless solution. The volatile materials were

then removed under dynamic vacuum at –60 °C for 3.5 h. The reactor was stored at –70 °C for 5 days and was then pumped on at room temperature for 1 h to afford a viscous green liquid (0.037 g, 0.14 mmol, 98 % with respect to MoOF$_4$). NMR (ppm, CH$_2$Cl$_2$, 300 MHz, room temperature, unlocked): ^{19}F 141.50 (s, MoOF$_4$(NC$_5$H$_5$); ^1J(Mo–F) = 68.8 Hz). ^{1}H 7.94 (dd, H$_o$, ^3J(H$_o$–H$_m$) = 4.9 Hz, ^4J(H$_o$–H$_p$ = 1.7 Hz); 7.29 (tt, H$_p$, ^3J(H$_p$–H$_m$) = 7.6 Hz) 6.86 (dd, H$_m$). ^{13}C{^{1}H} 146.44 (C$_o$), 139.08 (C$_p$), 124.14 (C$_m$).

MoF$_5$(NCCH$_3$). In the dry box, a ¼ in. o.d. FEP reactor was loaded with MoF$_5$ (0.0462 g, 0.242 mmol). Acetonitrile (0.713 g, 17.4 mmol) was the distilled into the reactor at –196 °C. Warming the reactor to –40 °C afforded a colourless solution upon gentle agitation. The reactor was allowed to stand at –40 °C for 1 h and was then stored at –60 °C for 16 h. The volatile materials were removed under dynamic vacuum at –35 °C for 2 h and at room temperature for 30 min to afford a fine, cream-coloured powder (0.057 g, 0.246 mmol, expected 0.0561 g). A trace impurity of MoOF$_4$(NCCH$_3$) (δ = 147.52 ppm (s)) was identified by ^{19}F NMR spectroscopy (CH$_3$CN, 300 MHz, room temperature, unlocked).

Preparation of Samples for EPR Spectroscopy. *MoF$_5$(NC$_5$H$_5$)$_2$ in Adamantane.* Adamantane was purified via sublimation at 100 °C over 1 h. In the dry box, a portion of the adamantane (0.5757 g, 4.23 mmol) was transferred into a mortar and ground into a fine white powder. MoF$_5$(NC$_5$H$_5$)$_2$ (0.0096 g 0.027 mmol) was added to the mortar, and the mixture was ground thoroughly to afford a light pink powder (1.7 wt. %), which was subsequently loaded into a 4 mm o.d. FEP reactor for EPR spectroscopy.

MoF$_5$(NC$_5$H$_5$)$_2$ in MoOF$_4$(NC$_5$H$_5$)$_2$. In the dry box, a ¼ in. o.d. FEP reactor was loaded with MoOF$_4$ (0.1606 g, 0.8546 mmol) and MoF$_5$ (0.0015 g, 0.0079 mmol). Once the reactor was removed from the dry box, it was immediately cooled to –30 °C prior to the distillation of pyridine

(0.923 g) at −196 °C. Upon warming the reactor to − 35 °C, a mustard yellow suspension formed immediately and traces of light pink solid were also observed. The reactor was vigorously agitated and sonicated over 20 min to afford a thick, faint pink suspension. The volatile materials were then removed under dynamic vacuum at −25 °C for 30 min and at room temperature for 10 min, yielding a light pink solid mixture (0.93 wt. %). The powder was transferred into a 4 mm o.d. FEP reactor for EPR spectroscopy.

[MoF$_5$(NC$_5$H$_5$)]$_2$ in Adamantane. In the dry box, purified adamantane (0.1503 g, 1.103 mmol) was transferred into a mortar and ground in to a fine white powder. [MoF$_5$(NC$_5$H$_5$)]$_2$ (0.0015 g, 0.0028 mmol) was added to the mortar, and the mixture was ground thoroughly to afford a white mixture (1.0 wt. %), which was subsequently loaded into a 4 mm o.d. FEP reactor for EPR spectroscopy. Since only a weak signal was observed in the EPR spectrum at room temperature, an additional 0.0070 g (0.013 mmol) of [MoF$_5$(NC$_5$H$_5$)]$_2$ was added to the mixture to increase the concentration (5.7 wt. %). EPR spectroscopy was reattempted using the more concentrated sample, but no significant increase in the intensity of the rhombic trace was observed.

MoF$_5$(NCCH$_3$) in Adamantane. In the dry box, purified adamantane (0.2176 g, 1.597 mmol) was transferred into a mortar and ground into a fine white powder. MoF$_5$(NCCH$_3$) (0.0014 g, 0.0060 mmol) was added to the mortar, and the mixture was ground thoroughly to afford a white mixture (0.64 wt. %), which was subsequently loaded into a 4 mm o.d. FEP reactor for EPR spectroscopy. Since no signal attributable to MoF$_5$(NCCH$_3$) was observed in the EPR spectrum at room temperature, an additional 0.0027 g (0.012 mmol) of MoF$_5$(NCCH$_3$) was added to the mixture to increase the concentration (1.9 wt. %). EPR spectroscopy was reattempted using the more concentrated sample, but no signal attributable to MoF$_5$(NCCH$_3$) was observed, even upon cooling to −155 °C.

X-ray Crystallography. Once the volatile materials were removed under dynamic vacuum, reactors were cut on an aluminum trough cooled to between $-50\,°C$ to $-80\,°C$ by a stream of dry N_2, which was generated by passing the gas through a Dewar of liquid N_2. The crystals were deposited onto the trough, and selected crystals were affixed to a Nylon cryo-loop coated in perfluorinated polyether oil (Fomblin Z-25) and quickly transferred to the goniometer using liquid-N_2-cooled cryotongs.

Data Collection and Reduction. The crystals were centered on a Rigaku SuperNova diffractometer equipped with a Dectris Pilatus 3R 200K-A hybrid-pixel-array detector, a four-circle κ goniometer, an Oxford Cryostream 800, and sealed MoKα and CuKα X-ray sources. Data were collected using the MoKα source ($\lambda = 0.71073$ Å) at $-173\,°C$. Crystals were screened for quality before a pre-experiment was run to determine the unit cell, and a data-collection strategy was calculated based on the determined unit cell and intensity of the preliminary data. This strategy was optimised to collect five-fold redundant data at a resolution of 0.77 Å. The data were processed using CrysAlisPro,[63] which applied necessary Lorentz and polarization corrections to the integrated data and scaled the data. A numerical (Gaussian-grid) absorption correction was generated based upon the indexed faces of the crystal.

Structure Solution and Refinement. Atom positions were determined using the intrinsic phasing method (ShelXT)[64] and were refined using least-squares refinement (ShelXL).[65] Non-hydrogen atoms were refined anisotropically and recommended weights for the atoms were determined before hydrogen atoms were introduced using a riding model (HFIX). The maximum and minimum electron density in the Fourier difference maps were located close to the molybdenum atoms. Structure solution and refinement were performed with the aid of Olex2

(version 1.2).[66] The disorder of the anion in $[C_5H_5NH]_3[Mo_2O_2F_9]$ was modelled as a two-component disorder (50:50). Refinement in the lower-symmetry space group (P1) gave the same disorder and did not improve the model.

Raman Spectroscopy. All Raman spectra were recorded on solid samples in flame-sealed glass melting point capillaries, with the exception of $MoOF_4(NC_5H_5)$ and the frozen solutions of $MoF_5(NC_5H_5)$, for which Raman data was collected in ¼ in. o.d. FEP reactors. Spectra were recorded at room temperature and at -100 °C using a Bruker RFS-100 Raman spectrometer outfitted with a quartz beam-splitter and liquid-N_2-cooled germanium detector. The 1064-nm line of a Nd:YAG laser was used for excitation of the sample, and back-scattered (180°) radiation was sampled. The usable Stokes range of the collected data was 85 to 3500 cm^{-1} with a spectral resolution of 2 cm^{-1}. The laser power was set to 150 mW.

NMR Spectroscopy. All NMR spectra were recorded in heat-sealed 4-mm o.d. FEP tubes in 5-mm o.d. glass inserts using a Bruker Avance II 300 MHz spectrometer equipped with a 5-mm broadband probe. Spectra were recorded unlocked on dilute CH_2Cl_2, CH_3CN, or SO_2 solutions and were referenced externally to neat $CFCl_3$ (^{19}F) or $Si(CH_3)_4$ (^1H and $^{13}C\{^1H\}$) at 20 °C.

EPR Spectroscopy. All EPR spectra were recorded in 4 mm o.d. FEP tubes sealed with stainless steel valves, with the exception of the liquid helium experiment for $MoF_5(NC_5H_5)_2$, for which a 3 mm o.d. quartz tube was employed. Measurements were taken with a Bruker EMX Plus spectrometer equipped with ER 073 10" magnet, ER 083B-4Q 12 kW power supply X-band Ultra Low Noise microwave bridge and Bruker High Sensitivity Probehead. Spectra were recorded in 20 °C increments between room temperature and -155 °C using the ER 4141VT-UM liquid nitrogen variable-temperature system. For the liquid helium experiment, the Bruker ER 4112HV cryostat and Oxford Instruments controller were used. A constant temperature of -263 ± 0.2 °C

was maintained during spectral scans. In all experiments, wide and focussed scan widths, and variation in applied power and modulation amplitude were systematically employed to obtain the best possible spectra for each sample and temperature.

The experimental EPR spectra recorded at −155 °C were used in combination with EasySpin[67] to generate and fit simulated spectra. For the spectrum of $MoF_5(NC_5H_5)_2$ in powdered adamantane (Figure 9), the g-values computed by ORCA were used as initial values, and the Nelder/Mead downhill simplex algorithm was used to fit the experimental spectrum. Once a good fit had been achieved, a second spin system was specified using the g-values of the axial FEP signal (determined from a separate experiment) and was included in the simulation. The relative weight of the two systems was allowed to vary until a new best fit was achieved. No nuclear spins were specified during the fitting of the $MoF_5(NC_5H_5)_2$ in powdered adamantane spectrum.

Fitting the experimental spectrum of $MoF_5(NC_5H_5)_2$ in the $MoOF_4(NC_5H_5)_2$ host (Figure 11) was more complicated. Due to the size of the spin system in this molecule, the default method of full matrix diagonalization in EasySpin could not be utilized whilst including all of the nuclei calculated to have significant spin density, as even a single spectrum could not be generated after several hours of simulation. To enable the use of the least-squares fitting function by sufficiently reducing the time required to generate simulations, second-order perturbation theory was employed as the simulation method. Additionally, a user-defined function was applied to constrain the fitting of hyperfine tensors for sets of symmetry equivalent nuclei; the A-values of equatorial fluorine atoms were constrained to remain equal, as were those of the axial fluorine atoms. An initial spectrum was generated using the g-values measured from the spectrum of $MoF_5(NC_5H_5)_2$ in powdered adamantane and the A-values computed by ORCA. This initial fit demonstrated some inconsistencies with the experimental spectrum that were not resolvable either by altering

simulation algorithm or rmsd residual target. Using only the on-diagonal components, some of the A-values were manually altered to obtain a closer visual fit with the spectrum before resuming fitting. The manual alterations were performed by measuring splitting on the experimental spectrum and altering the closest A-value of the same orientation to match. The final simulated spectrum was achieved by using this manually altered spectrum as a starting point and fitting to the experimental spectrum by employing the particle swarm algorithm followed by the Nelder/Mead downhill simplex algorithm. All of the values reported in Table 7 were allowed to vary with the exception of Axyz(F1), which were not included in the simulation due to their small contribution to the splitting pattern and significant deficit to simulation time.

Computational Methods. Optimization and frequency calculations were performed in the gas phase using the DFT/B3LYP level of theory, as implemented in Gaussian 16 (revision B.01).[68] The aug-cc-pVTZ basis set and associated Stuttgart pseudopotentials were used for molybdenum,[69] whereas the aug-cc-pVTZ basis set was used for nitrogen, oxygen and fluorine, and the cc-pVTZ basis set was used for carbon and hydrogen. This combined basis set is denoted as aVTZ. Basis set parameters were obtained from the EMSL Basis Set Exchange.[70,71] Geometry optimizations were performed using analytic-gradient methods, and all subsequent calculations (with the exception of one variant of the EPR parameter calculations) were performed using the optimized geometries. Whenever possible, the experimental geometries were used as starting points for the geometry optimizations. No significant spin contamination resulted from the unrestricted calculations employed for the open shell (d^1) systems. The NBO analyses were conducted using NBO (version 6.0),[72] and GaussView (version 6.0)[73] was used to visualize the vibrational modes and facilitate their description.

Computation of EPR g- and A-values was undertaken with ORCA 4.2.1 using the ZORA framework.[74,75] The application of a GGA-based exchange-correlation functional for DFT-predicted g-tensors was informed by a computational study conducted by Hadt et al., who found that such functionals provide the best agreement between the calculated and experimental values for related Mo^V oxide fluorides.[18] Both PBE and BPW91 gradient-corrected DFT functionals were employed in concert with recently-published all-electron relativistically-corrected basis sets for Mo and the EPR-III and IGLO-III bases for light elements. The results selected, somewhat arbitrarily, as the starting points for fitting of the broad-line and hyperfine-split EPR spectra (see previous section) are from BPW91/{F,N,O:IGLO-III,Mo:SARC-ZORA-TZVP}.[52] The geometries used for the EPR parameter calculations include those derived from the B3LYP-geometry optimization, as well as the X-ray structure after constraining it to exact C_2 using the Point Symmetry tool in GaussView.

ASSOCIATED CONTENT

Supporting Information. The Supporting Information is available free of charge at https://pubs.acs.org.

Crystallographic and calculated bond lengths and angles; NMR spectra; optimized geometries; experimental and calculated vibrational frequencies and Raman spectra; EPR spectra and additional EPR discussion; selected orbital energies; data from NBO analyses (PDF)

Accession Codes

CCDC 2099017-2099021 contain the supplementary crystallographic data for this paper. These data can be obtained free of charge via www.ccdc.cam.ac.uk/data_request/cif, or by emailing

REFERENCES

(1)   Haartz, J. C.; McDaniel, D. H. Fluoride Ion Affinity of Some Lewis Acids. *J. Chem. Soc.* **1973**, *95* (26), 8562–8565.
(2)   Christe, K. O.; Dixon, D. A.; McLemore, D.; Wilson, W. W.; Sheehy, J. A.; Boatz, J. A. On a Quantitative Scale for Lewis Acidity and Recent Progress in Polynitrogen Chemistry. *J. Fluorine Chem.* **2000**, *101* (2), 151–153.
(3)   Hwang, I. C.; Seppelt, K. Gold Pentafluoride: Structure and Fluoride Ion Affinity. *Angew. Chem., Int. Ed.* **2001**, *40* (19), 3690–3693.
(4)   Benjamin, S. L.; Levason, W.; Reid, G. Medium and High Oxidation State Metal/Non-Metal Fluoride and Oxide–Fluoride Complexes with Neutral Donor Ligands. *Chem. Soc. Rev.* **2013**, *42* (4), 1460–1499.
(5)   Levason, W.; Monzittu, F. M.; Reid, G. Coordination Chemistry and Applications of Medium/High Oxidation State Metal and Non-Metal Fluoride and Oxide-Fluoride Complexes with Neutral Donor Ligands. *Coord. Chem. Rev.* **2019**, *391*, 90–130.
(6)   Stene, R. E.; Scheibe, B.; Pietzonka, C.; Karttunen, A. J.; Petry, W.; Kraus, F. MoF_5 Revisited. A Comprehensive Study of MoF_5. *J. Fluorine Chem.* **2018**, *211*, 171–179.
(7)   Stene, R.; Scheibe, B.; Ivlev, S. I.; Karttunen, A. J.; Petry, W.; Kraus, F. Photochemical Synthesis of Tungsten Pentafluoride, WF_5. *Anorg. Allg. Chem.* **2021**, *647* (4), 218–224.
(8)   Peacock, R. D. Two New Fluorides of Molybdenum. *Proc. Chem. Soc.* **1957**, 59.
(9)   Schröder, J.; Grewe, F. J. Preparation of Tungsten Pentafluoride. *Angew. Chem., Int. Ed. Engl.* **1968**, *7* (2), 132–133.
(10)   Craciun, R.; Picone, D.; Long, R. T.; Li, S.; Dixon, D. A.; Peterson, K. A.; Christe, K. O. Third Row Transition Metal Hexafluorides, Extraordinary Oxidizers, and Lewis Acids: Electron Affinities, Fluoride Affinities, and Heats of Formation of WF_6, ReF_6, OsF_6, IrF_6, PtF_6, and AuF_6. *Inorg. Chem.* **2010**, *49* (3), 1056–1070.
(11)   Craciun, R.; Long, R. T.; Dixon, D. A.; Christe, K. O. Electron Affinities, Fluoride

Affinities, and Heats of Formation of the Second Row Transition Metal Hexafluorides: MF_6 (M = Mo, Tc, Ru, Rh, Pd, Ag). *J. Phys. Chem. A* **2010**, *114* (28), 7571–7582.

(12) Müller, L. O.; Himmel, D.; Stauffer, J.; Steinfeld, G.; Slattery, J.; Santiso-Quiñones, G.; Brecht, V.; Krossing, I. Simple Access to the Non-Oxidizing Lewis Superacid PhF→Al(OR^F)$_3$ (R^F =C(CF$_3$)$_3$). *Angew. Chem., Int. Ed.* **2008**, *47* (40), 7659–7663.

(13) Stene, R. E.; Scheibe, B.; Petry, W.; Kraus, F. Synthesis and Characterization of the Hexafluoridomolybdates(V) A[MoF$_6$] (A = Li–Cs). *Eur. J. Inorg. Chem.* **2020**, *2020* (19), 1834–1843.

(14) Mercer, M.; Ouellette, T. J.; Ratcliffe, C. T.; Sharp, D. W. A. Preparation and Complexes of Molybdenum Pentafluoride and Molybdenum(V) Bromide Tetrafluoride. *J. Chem. Soc. A Inorg. Phys. Theor.* **1969**, 2532.

(15) Fuggle, J. C.; Sharp, D. W. A.; Winfield, J. M. Niobium, Tantalum and Molybdenum Pentafluoride Complexes with Organic Ligands. *J. Fluorine Chem.* **1972**, *1* (4), 427–431.

(16) Sunil, K. K.; Rogers, M. T. ESR Studies of Some Oxotetrahalo Complexes of Vanadium(IV) and Molybdenum(V). *Inorg. Chem.* **1981**, *20* (10), 3283–3287.

(17) Manoharan, P. T.; Rogers, M. T. Ligand Hyperfine Interactions in Molybdenyl and Chromyl Halide Complexes. *J. Chem. Phys.* **1968**, *49* (12), 5510–5519.

(18) Hadt, R. G.; Nemykin, V. N.; Olsen, J. G.; Basu, P. Comparative Calculation of EPR Spectral Parameters in [Mo^{V}OX$_4$]$^-$, [Mo^{V}OX$_5$]$^{2-}$, and [Mo^{V}OX$_4$(H$_2$O)]$^-$ Complexes. *Phys. Chem. Chem. Phys.* **2009**, *11* (44), 10377–10384.

(19) Hille, R. The Mononuclear Molybdenum Enzymes. *Chem. Rev.* **1996**, *96* (7), 2757–2816.

(20) El-Kurdi, S.; Al-Terkawi, A.-A.; Schmidt, B. M.; Dimitrov, A.; Seppelt, K. Tungsten(VI) and Tungsten(V) Fluoride Complexes. *Chem. Eur. J.* **2010**, *16* (2), 595–599.

(21) Turnbull, D.; Hazendonk, P.; Wetmore, S. D.; Gerken, M. Stabilisation of [WF$_5$]$^+$ and WF$_5$ by Pyridine: Facile Access to [WF$_5$(NC$_5$H$_5$)$_3$]$^+$ and WF$_5$(NC$_5$H$_5$)$_2$. *Chem. Eur. J.* **2020**, *26* (30), 6879–6886.

(22) Bao, N.; Winfield, J. M. Oxidation of Molybdenum and Tungsten Metals by Molybdenum and Tungsten Hexafluorides in Acetonitrile. Preparation of the 1:1 Pentafluoride Acetonitrile Complexes. *J. Fluorine Chem.* **1990**, *50* (3), 339–343.

(23) Turnbull, D.; Wetmore, S. D.; Gerken, M. Stabilisation of [W^{V}F$_4$]$^+$ by N- and P-Donor Ligands: Second-Order Jahn-Teller Effects in Octacoordinate d^1 Complexes. *Chem. Eur. J.* **2021**.

(24) Turnbull, D.; Chaudhary, P.; Leenstra, D.; Hazendonk, P.; Wetmore, S. D.; Gerken, M. Reactions of Molybdenum and Tungsten Oxide Tetrafluoride with Sulfur(IV) Lewis Bases: Structure and Bonding in [WOF$_4$]$_4$, MOF$_4$(OSO), and [SF$_3$][M$_2$O$_2$F$_9$] (M = Mo, W). *Inorg. Chem.* **2020**, *59* (23), 17544–17554.

(25) Stene, R. E.; Scheibe, B.; Karttunen, A. J.; Petry, W.; Kraus, F. Lewis Acidic Behavior of MoOF$_4$ towards the Alkali Metal Fluorides in Anhydrous Hydrogen Fluoride Solutions. *Eur. J. Inorg. Chem.* **2019**, *2019* (32), 3672–3682.

(26) Levason, W.; Monzittu, F. M.; Reid, G.; Zhang, W.; Hope, E. G. Complexes of Molybdenum(VI) Oxide Tetrafluoride and Molybdenum(VI) Dioxide Difluoride with Neutral N- and O-Donor Ligands. *J. Fluorine Chem.* **2017**, *200*, 190–197.

(27) Levason, W.; Reid, G.; Zhang, W. Coordination Complexes of the Tungsten(VI) Oxide Fluorides WOF$_4$ and WO$_2$F$_2$ with Neutral Oxygen- and Nitrogen-Donor Ligands. *J. Fluorine Chem.* **2016**, *184*, 50–57.

(28) Emsley, J. W.; Levason, W.; Reid, G.; Zhang, W.; De Luca, G. Phosphine and

Diphosphine Complexes of Tungsten(VI) Oxide Tetrafluoride. *J. Fluorine Chem.* **2017**, *197*, 74–79.

(29)   Bond, A. M.; Irvine, I.; O'Donnell, T. A. Electrochemical Studies of Molybdenum Hexafluoride and Related Compounds in Anhydrous Hydrogen Fluoride. *Inorg. Chem.* **1977**, *16* (4), 841–844.

(30)   Schröder, J.; Grewe, F. J. Darstellung und Eigenschaften von Wolframpentafluorid. *Chem. Ber.* **1970**, *103* (5), 1536–1546.

(31)   Paine, R. T.; Asprey, L. B. Reductive Fluoride Elimination Synthesis of Transition Metal Fluorides. Synthesis of Molybdenum Pentafluoride and Molybdenum Tetrafluoride. *Inorg. Chem.* **1974**, *13* (6), 1529–1531.

(32)   Arnaudet, L.; Bougon, R.; Ban, B.; Charpin, P.; Isabey, J.; Lance, M.; Nierlich, M.; Vigner, J. Preparation, Characterization, and Crystal Structure of The Adducts $WOF_4 \cdot nC_5H_5N$ (n = 1, 2). *Inorg. Chem.* **1989**, *28* (2), 257–262.

(33)   Craciun, R.; Dixon, D. A. private communication.

(34)   Turnbull, D.; Wetmore, S. D.; Gerken, M. Synthesis, Characterization, and Lewis Acid Behavior of $[W(NC_6F_5)F_4]_x$ and Computational Study of $W(NR)F_4$ (R = H, F, CH_3, CF_3, C_6H_5, C_6F_5), $W(NC_6F_5)F_4(NCCH_3)$, and $W(NC_6F_5)F_4(NC_5H_5)_n$ (n = 1, 2). *Inorg. Chem.* **2019**, *58* (9), 6363–6375.

(35)   Giese, S.; Seppelt, K. Structural Principles in Seven-Coordinate Subgroup Compounds: The Complex Anions MoF_7^-, WF_7^-, and $ReOF_6^-$. *Angew. Chem., Int. Ed. Engl.* **1994**, *33* (4), 461–463.

(36)   Haiges, R.; Deokar, P.; Christe, K. O. Adduct Formation of Tantalum(V)- and Niobium(V) Fluoride with Neutral Group 15 Donor Ligands, an Example for Ligand Induced Self-Ionization. *Z. Anorg. Allg. Chem.* **2014**, *640* (8–9), 1568–1575.

(37)   Opalovskii, A. A.; Khaldoyanidi, K. A. Autoionization and Complex Formation of Molybdenum Pentafluoride in a Melt. *Bull. Acad. Sci. USSR Div. Chem. Sci.* **1973**, *22* (2), 270–272.

(38)   Mattes, R.; Mennemann, K.; Jäckel, N.; Rieskamp, H.; Brockmeyer, H.-J. Structure and Properties of the Fluorine-Rich Oxofluoromolybdates $Cs_3[Mo_2O_6F_3]$, $(NH_4)_3[Mo_2O_2F_9]$ and $(NH_4)_2[MoOF_5]$. *J. Less Common Met.* **1980**, *76* (1–2), 199–212.

(39)   Leimkühler, M.; Buchholz, N.; Mattes, R. Zwei- und Dreikernige Fluorooxoanionen des Molybdäns und Wolframs. Kristallstrukturen von $K_2(NMe_4)[Mo^V_2O_2F_9] \cdot H_2O$ und $(NMe_4)_2[Mo^{VI}_2O_4F_6(H_2O)]$. *Z. Naturforsch. Sect. B J. Chem. Sci.* **1989**, *44* (4), 389–394.

(40)   Du, Y.; Yang, M.; Yu, J.; Pan, Q.; Xu, R. An Unexpected Photoelectronic Effect from $[Co(en)_3]_2(Zr_2F_{12})(SiF_6) \cdot 4H_2O$, a Compound Containing an H-Bonded Assembly of Discrete $[Co(en)_3]_3^+$, $(Zr_2F_{12})^{4-}$, and $(SiF_6)^{2-}$ Ions. *Angew. Chem., Int. Ed.* **2005**, *44* (48), 7988–7990.

(41)   Benjamin, S. L.; Levason, W.; Pugh, D.; Reid, G.; Zhang, W. Preparation and Structures of Coordination Complexes of the Very Hard Lewis Acids ZrF_4 and HfF_4. *Dalt. Trans.* **2012**, *41* (40), 12548–12557.

(42)   Batsanov, S. S. Van Der Waals Radii of Elements. *Inorg. Mater.* **2001**, *37* (9), 871–885.

(43)   Kiriazis, L.; Mattes, R.; Obst, F. Structure of Hexafluorotetrapyridine Dimolybdenum(III). *Inorg. Chim. Acta* **1991**, *181* (2), 157–159.

(44)   Hayatifar, M.; Marchetti, F.; Pampaloni, G.; Patil, Y.; Raspolli Galletti, A. M. Fluoride Adducts of Niobium(V): Activation Reactions and Alkene Polymerizations. *Inorg. Chim. Acta* **2013**, *399*, 214–218.

(45) Arnaudet, L.; Bougon, R.; Buu, B. Molecular Structure of the WOF4•2py (py = pyridine) Adduct as Refined by ^{19}F NMR Spectroscopy. *J. Fluorine Chem.* **1995**, *74* (2), 223–225.

(46) Arnaudet, L.; Bougon, R.; Ban, B.; Charpin, P.; Isabey, J.; Lance, M.; Nierlich, M.; Vigner, J. 2,2′-Bipyridyl Adducts of Tungsten Oxide Fluorides: Preparation and Characterization of WOF4•bipy and WO2F2•bipy; Crystal Structure of WO2F2•bipy . *Can. J. Chem.* **1990**, *68* (3), 507–512.

(47) Arnaudet, L.; Bougon, R.; Ban, B.; Lance, M.; Kaska, W. C. Adducts of Tungsten Oxide Tetrafluoride with 1,8-Naphthyridine and 2,7-Dimethyl-1,8-Naphthyridine: Preparation and Characterization of WOF4•napy and WOF4•dmnapy. *J. Fluorine Chem.* **1991**, *53* (2), 171−180.

(48) Klessinger, M.; Bolte, P. Hybridization and Valence Angle Dependence of Geminal NMR Coupling Constants. *J. Mol. Struct. (Theochem).* **1988**, *169*, 119–124.

(49) Nieboer, J.; Yu, X.; Chaudhary, P.; Mercier, H. P. A.; Gerken, M. Synthesis, Characterization, and Computational Study of WSF4•NC5H5. *Z. Anorg. Allg. Chem.* **2012**, *638* (3–4), 520–525.

(50) Beattie, I. R.; Livingston, K. M. S.; Reynolds, D. J.; Ozin, G. A. Vibrational Spectra of Some Oxide Halides of the Transition Elements with Particular Reference to Gas-Phase and Single-Crystal Raman Spectroscopy. *J. Chem. Soc. A Inorganic, Phys. Theor.* **1970**, No. 0, 1210–1216.

(51) Garif'yanov, N. S.; Fedotov, V. N.; Kucheryaenko, N. S. Electron Paramagnetic Resonance and Nuclear Spin Echo in Solutions of Oxyfluorides of Pentavalent Molybdenum. *Bull. Acad. Sci. USSR Div. Chem. Sci.* **1964**, *13* (4), 689–691.

(52) Rolfes, J. D.; Neese, F.; Pantazis, D. A. All-Electron Scalar Relativistic Basis Sets for the Elements Rb–Xe. *J. Comput. Chem.* **2020**, *41* (20), 1842–1849.

(53) Weil, J. W.; Boulton, J. R.; Wertz, J. E. *Electron Paramagnetic Resonance: Elementary Theory and Practical Applications.* Wiley: NY. 1994. p. 98.

(54) Holloway, J. H.; Hope, E. G.; Raynor, J. B.; Townson, P. T. Magnetic Resonance Studies on Osmium Pentafluoride Oxide. *J. Chem. Soc. Dalt. Trans.* **1992**, No. 7, 1131–1134.

(55) Mitov, S.; Hübner, G.; Brack, H.-P.; Scherer, G. G.; Roduner, E. *In situ* Electron Spin Resonance Study of Styrene Grafting of Electron Irradiated Fluoropolymer Films for Fuel Cell Membranes. *J. Polym. Sci. Part B Polym. Phys.* **2006**, *44* (23), 3323–3336.

(56) Rasmussen, K.; Grampp, G.; van Eesbeek, M.; Rohr, T. Thermal and UV Degradation of Polymer Films Studied In situ with ESR Spectroscopy. *ACS Appl. Mater. Interfaces* **2010**, *2* (7), 1879–1883.

(57) Yoshikawa, T.; Oshima, A.; Murakami, T.; Washio, M. ESR Study for Ion Beam Induced Phenomena in Poly(Tetrafluoroethylene-Co-Hexafluoropropylene) (FEP). *Rad. Phys. Chem.* **2012**, *81* (12), 1904–1909.

(58) Roessler, M. M.; Salvadori, E. Principles and Applications of EPR Spectroscopy in the Chemical Sciences. *Chem. Soc. Rev.* **2018**, *47* (8), 2534–2553.

(59) Hulliger, J.; Zoller, L.; Ammeter, J. H. Orientation Effects in EPR Powder Samples Induced by the Static Magnetic Field. *J. Magn. Reson.* **1982**, *48* (3), 512–518.

(60) Boys, S. F.; Bernardi, F. The Calculation of Small Molecular Interactions by the Differences of Separate Total Energies. Some Procedures with Reduced Errors. *Mol. Phys.* **1970**, *19* (4), 553–566.

(61) Winfield, J. M. Acetonitrile, a Convenient Solvent for Inorganic Fluorides. *J. Fluorine Chem.* **1984**, *25* (1), 91–98.

(62) Selig, H.; Sunder, W. A.; Shilling, F.C.; Falconer, W. E. Hydrolysis Reactions of Transition Metal Fluorides in Liquid Hydrogen Fluoride: Oxonium Salts with Nb, Ta and W. *J. Fluorine Chem.* **1978**, *11* (6), 629-635.

(63) *CrysAlisPro*, ver. 171.38.43; Agilent Technologies, Ltd.: Yarnton, Oxfordshire, England, 2014.

(64) Sheldrick, G. M. SHELXT − Integrated Space-Group and Crystal-Structure Determination. A*cta Crystallogr., Sect. A: Found. Adv.* **2015**, *71* (1), 3−8.

(65) Sheldrick, G. M. Crystal Structure Refinement with SHELXL. *Acta Crystallogr., Sect. C: Struct. Chem.* **2015**, *71* (1), 3−8.

(66) Dolomanov, O. V.; Bourhis, L. J.; Gildea, R. J.; Howard, J. A. K.;Puschmann, H. OLEX2 : A Complete Structure Solution, Refinement and Analysis Program. *J. Appl. Crystallogr.* **2009**, *42* (2), 339−341.

(67) Stoll, S.; Schweiger, A. EasySpin, a Comprehensive Software Package for Spectral Simulation and Analysis in EPR. *J. Magn. Reson.* **2006**, *178* (1), 42–55.

(68) Frisch, M. J.; Trucks, G. W.; Schlegel, H. B.; Scuseria, G. E.; Robb, M. A.; Cheeseman, J. R.; Scalmani, G.; Barone, V.; Petersson, G. A.; Nakatsuji, H.; Li, X.; Caricato, M.; Marenich, A. V.; Bloino, J.; Janesko, B. G.; Gomperts, R.; Mennucci, B.; Hratchian, H. P.; Ortiz, J. V.; Izmaylov, A. F.; Sonnenberg, J. L.; Williams-Young, D.; Ding, F.; Lipparini, F.; Egidi, F.; Goings, J.; Peng, B.; Petrone, A.; Henderson, T.; Ranasinghe, D.; Zakrzewski, V. G.; Gao, J.; Rega, N.; Zheng, G.; Liang, W.; Hada, M.; Ehara, M.; Toyota, K.; Fukuda, R.; Hasegawa, J.; Ishida, M.; Nakajima, T.; Honda, Y.; Kitao, O.; Nakai, H.; Vreven, T.; Throssell, K.; Montgomery, J. A., Jr.; Peralta, J. E.; Ogliaro, F.; Bearpark, M. J.; Heyd, J. J.; Brothers, E. N.; Kudin, K. N.; Staroverov, V. N.; Keith, T. A.; Kobayashi, R.; Normand, J.; Raghavachari, K.; Rendell, A. P.; Burant, J. C.; Iyengar, S. S.; Tomasi, J.; Cossi, M.; Millam, J. M.; Klene, M.; Adamo, C.; Cammi, R.; Ochterski, J. W.; Martin, R. L.; Morokuma, K.; Farkas, O.; Foresman, J. B.; Fox, D. J. Gaussian 16, rev. B.01; Gaussian, Inc.: Wallingford, CT, 2016.

(69) Peterson, K. A.; Figgen, D.; Dolg, M.; Stoll, H. Energy-Consistent Relativistic Pseudopotentials and Correlation Consistent Basis Sets for the 4*d* Elements Y–Pd. *J. Chem. Phys.* **2007**, *126* (12), 124101.

(70) Feller, D. The Role of Databases in Support of Computational Chemistry Calculations. *J. Comput. Chem.* **1996**, *17* (13), 1571–1586.

(71) Schuchardt, K. L.; Didier, B. T.; Elsethagen, T.; Sun, L.; Gurumoorthi, V.; Chase, J.; Li, J.; Windus, T. L. Basis Set Exchange: A Community Database for Computational Sciences. *J. Chem. Inf. Model.* **2007**, *47* (3), 1045–1052.

(72) Glendening, E. D.; Badenhoop, J. K.; Reed, A. E.; Carpenter, J.; E.; Bohmann, J. A.; Morales, C. M.; Landis, C. R.; Weinhold, F. *NBO*, ver. 6.0; Theoretical Chemistry Institute, University of Wisconsin: Madison, WI, 2013.

(73) Dennington, R.; Keith, T. A.; Millam, J. M. *GaussView*, ver. 6.0.; Semichem, Inc.: Shawnee Mission, KS, 2016.

(74) Neese, F. Software Update: The ORCA Program System, Version 4.0. *WIREs Comput. Mol. Sci.* **2018**, *8* (1), e1327.

(75) Neese, F. Quantum Chemistry and EPR Parameters. *eMagRes*. **2017**, *6*, 1–22.

Table of Contents Synopsis and Graphic

The Lewis acid chemistry of MoF$_5$ was investigated towards C$_5$H$_5$N and CH$_3$CN, affording MoF$_5$(NCCH$_3$) and MoF$_5$(NC$_5$H$_5$)$_n$ (n = 1, 2), which represent the first conclusively characterized neutral adducts of MoF$_5$. For comparison, the analogous d^0 MoOF$_4$(NC$_5$H$_5$)$_n$ adducts were synthesized, and the structures of all C$_5$H$_5$N adducts were elucidated via X-ray crystallography as well as DFT calculations. Paramagnetic MoF$_5$(NC$_5$H$_5$)$_2$ was characterized by EPR spectroscopy, and multinuclear NMR spectroscopy revealed a unprecedented isomerism for MoOF$_4$(NC$_5$H$_5$)$_2$ in solution.
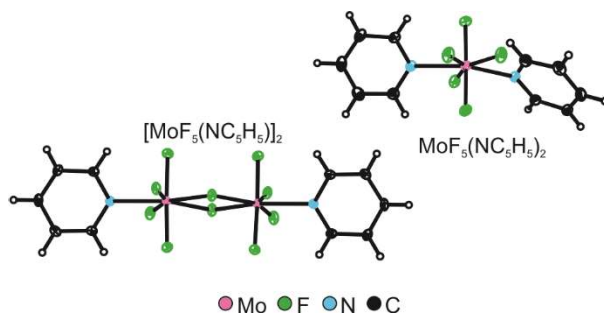
For Table of Contents only.